J. Fluid Mech. (2009), *vol.* 623, *pp.* 27–58.
doi:10.1017/S0022112008004825 Printed in the United Kingdom

Streamwise evolution of longitudinal vortices in a turbulent boundary layer

OLA LÖGDBERG[1,2], JENS H. M. FRANSSON[1]† AND P. HENRIK ALFREDSSON[1]

[1]Linné Flow Centre, KTH Mechanics, SE-100 44 Stockholm, Sweden

[2]Scania CV, SE-151 87 Södertälje, Sweden

(Received 28 February 2008 and in revised form 17 November 2008)

In this experimental study both smoke visualization and three-component hot-wire measurements have been performed in order to characterize the streamwise evolution of longitudinal counter-rotating vortices in a turbulent boundary layer. The vortices were generated by means of vortex generators (VGs) in different configurations. Both single pairs and arrays in a natural setting as well as in yaw have been considered. Moreover three different vortex blade heights h, with the spacing d and the distance to the neighbouring vortex pair D for the array configuration, were studied keeping the same d/h and D/h ratios. It is shown that the vortex core paths scale with h in the streamwise direction and with D and h in the spanwise and wall-normal directions, respectively. A new peculiar 'hooklike' vortex core motion, seen in the cross-flow plane, has been identified in the far region, starting around $200h$ and $50h$ for the pair and the array configuration, respectively. This behaviour is explained in the paper. Furthermore the experimental data indicate that the vortex paths asymptote to a prescribed location in the cross-flow plane, which first was stated as a hypothesis and later verified. This observation goes against previously reported numerical results based on inviscid theory. An account for the important viscous effects is taken in a pseudo-viscous vortex model which is able to capture the streamwise core evolution throughout the measurement region down to $450h$. Finally, the effect of yawing is reported, and it is shown that spanwise-averaged quantities such as the shape factor and the circulation are hardly perceptible. However, the evolution of the vortex cores are different both between the pair and the array configuration and in the natural setting versus the case with yaw. From a general point of view the present paper reports on fundamental results concerning the vortex evolution in a fully developed turbulent boundary layer.

1. Introduction

1.1. *Background and motivation*

This work deals with the development of streamwise vortices in turbulent boundary layers. Vortices are introduced in a controlled way by vortex generators (VGs), and their downstream development is investigated. The interest in such development is twofold: firstly because of the appearance of streamwise vortices in many natural flow situations and secondly because of the use of VGs to control separation.

† Email address for correspondence: jensf@mech.kth.se

In laminar and turbulent boundary layers along concave surfaces streamwise-oriented vortices develop, usually called Görtler vortices (see e.g. Swearingen & Blackwelder 1987). Also boundary layers influenced by spanwise rotation may develop streamwise-oriented vortices (Watmuff, Witt & Joubert 1985). In these two cases centrifugal and Coriolis forces, respectively, give rise to the vortices.

Surface roughness in laminar boundary layers may also generate streamwise vortices, which develop into longitudinal streaks of high and low velocities. Depending on the roughness height Reynolds number and spanwise distribution they may either promote or delay transition (Fransson *et al.* 2005, 2006). In turbulent boundary layers streamwise-oriented streaky structures of low and high velocities are well documented and are believed to be associated with streamwise vortices (Blackwelder & Eckelmann 1979).

As mentioned above the introduction of streamwise vortices through VGs can be used in order to delay or even avoid separation in adverse pressure gradient (APG) flows. Such devices are commonly observed on aircraft wings, diffusers and other APG surfaces but also have a potential to be used on ground vehicles. The work presented here is partly motivated by the possibility to reduce drag on trucks, by adding a boat tail to the rear and hence reducing the pressure drag. However, there is a restriction, prescribed by law, on how long the tail can be, and hence the deflection angle becomes an important parameter. Too large angles would give flow separation, which may be avoided by means of passive VGs. For design optimization fundamental knowledge of vortex evolution and induced drag is therefore needed. Here, we have chosen a fundamental study philosophy by idealizing the flow geometry to a zero pressure gradient (ZPG) turbulent boundary layer over a flat plate. This less complex flow geometry, compared to practical flow situations, allows us to focus on the fluid physics to a higher degree. One should however be careful in drawing conclusions for the APG case based on the present ZPG investigation, since the results are believed to depend on the pressure gradient to some degree.

Although naturally developing vortices are of interest in their own right we will only review the literature in which vortices are introduced into the boundary layer with some kind of vane-type VG, either to study the effect on separation directly or to study the vortex development in itself.

1.2. *Review of streamwise vortex development work*

The first experiments on conventional vane-type passive VGs were reported by Taylor (1947). This type of VG normally consists of a row of blades or airfoils mounted perpendicular to the surface and with an angle against the oncoming flow. The height (h) of these blades is often slightly higher than the boundary layer thickness (δ).

Schubauer & Spangenberg (1960) tried a variety of wall-mounted devices to increase the mixing in the boundary layer. They did this in different adverse pressure gradients and concluded that the effect of mixing is equivalent to a decrease in pressure gradient. One year later Pearcy (1961) published a VG design guide. The focus of this work was primarily on shock-wave boundary layer interaction and how to reduce the separation strength behind the shock wave. However, the study also deals with the basics of VGs, such as co- and counter-rotating vortex pairs (see figure 1 for definitions) as well as various geometrical parameters and shapes. In general, the co-rotating arrays are more efficient in preventing separation; however, for blade spacings greater than three times their height Pearcy (1961) showed that the counter-rotating arrays are equally good.

Pearcy (1961) also analysed the movement of the streamwise vortices inside the boundary layer, using the inviscid analysis of Jones (1957). That analysis, which takes

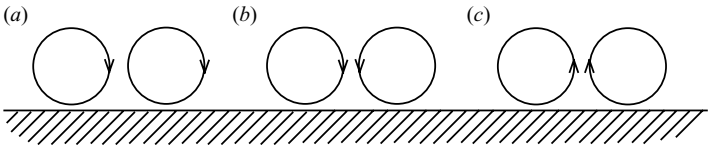

FIGURE 1. Different types of vortex pairs: (*a*) co-rotating, (*b*) counter-rotating with common downflow and (*c*) counter-rotating with common upflow.

into account the mirror imaging of the vortex at the wall, shows that the vortices move away from the wall infinitely as they are convected downstream. Vortices in a counter-rotating pair with a common downflow, arranged in a larger array, will first move away from each other and towards the wall. As the vortex is getting closer to the next vortex originating from the neighboring vortex pair it will be lifted away from the wall and asymptote to a constant in the spanwise direction. A new counter-rotating pair with common upflow is formed, which will continue to move away from the wall.

The evolution of a single vortex embedded in a turbulent boundary layer was thoroughly investigated by Shabaka, Mehta & Bradshaw (1985). The experimental results show that close to the wall the vortex induces vorticity, whose sign is opposite to that of the primary vortex. This induced vorticity was observed to be convected to the upwash side of the vortex. It is also stated that since turbulence is responsible for the diffusion of both the boundary layer and the vortices, their size ratio stays constant when moving downstream over the plate.

In a continuation Mehta & Bradshaw (1988) reported experiments with a counter-rotating vortex pair in the same basic set-up. The vortices had a common upflow from the surface and were initially embedded in the boundary layer, but due to the lift-up motion the vortex centres had moved to around twice the boundary layer thickness from the wall at a certain downstream distance. Compared to the single vortex configuration the circulation of each vortex is about 20 % stronger, which may be attributed to the constraint imposed of vortices acting as mirror images of each other. Throughout the test region there was little direct interaction between the vortices. Both in this study as well as in the study of the single vortex configuration the lateral meandering was shown to be small.

Another study of a single vortex in a boundary layer was performed by Westphal, Pauley & Eaton (1987). The vortex was produced by a delta wing that was slightly higher than the boundary layer thickness. They examined the vortex core area growth showed that when the core radius reaches a certain fraction of the height of the vortex centre to the wall, the vorticity contours become elliptic in shape. This was hypothesized to be a sign of meandering, but no evidence of any lateral movement of the vortices was found. The overall circulation, when the vortex evolved downstream, either decreased slowly or remained almost constant, depending on the case. The APG results are reported both in Westphal, Eaton & Pauley (1985) and Westphal *et al.* (1987) and show an increased diffusion of vorticity and hence a more rapid vortex centre growth. The onset of vorticity contour flattening was accelerated by the pressure gradient. To investigate more thoroughly whether the ellipticity was caused by vortex meandering an experiment with a laterally oscillating VG was carried out by Westphal & Mehta (1989). The results indicate that the unforced vortex is laterally stable and also show that the initial meandering caused by the moving VG is damped as the vortex is convected downstream.

Pauley & Eaton (1988) examined the streamwise development of pairs and arrays of longitudinal vortices embedded in a ZPG turbulent boundary layer. In this study the blade spacing of VGs and the blade angle were varied, and the difference between counter-rotating vortices, with common upflow and downflow, and co-rotating vortices were examined. All configurations use blade heights well above the boundary layer thickness. The researchers state that the interaction of the secondary flow and the wall produces negative vorticity below the vortex. This vorticity is swept up on the side of the primary vortex to create a small region of opposite vorticity. The vortex centre movements in the cross-plane are as expected from inviscid theory, although the paths are slightly modified by secondary flow structures. The proximity of other vortices does not affect circulation decay but increases the diffusion of vorticity.

In most experiments the first measurements are taken at more than $10h$ downstream of the VGs. In order to study the initial circulation and peak vorticity Wendt (2001) measured as close as one chord length downstream of the blade trailing edge of an array of VGs. Several counter- and co-rotating configurations were investigated by varying the aspect ratio, the blade length and the blade angle. The vortex strength was observed to be proportional to the free stream velocity, the blade angle and the ratio of the blade height and boundary layer thickness. With these three parameters held constant an increasing blade aspect ratio reduces circulation. In the study counter-rotating vortices show greater magnitudes of circulation than a single vortex produced with the same blade parameters. For co-rotating vortices the produced circulation is lower than for the single vortex. The circulation is shown to be accurately modelled by modified version of Prandtl's relation between circulation and airfoil geometry. In a previous work Wendt, Reichert & Jeffry (1995) studied the decay of counter-rotating vortices in approximately the same set-up. The vortices had their common flow directed upwards, and their distance to the wall increased as they evolved downstream. Thus the wall friction decreased, and the decay also decreased. The circulation decay is almost linear until a distance of $70h$ downstream the VG.

In most of the earlier studies VGs with $h/\delta > 1$ have been used. However to reduce the drag penalty caused by the VGs, work has been done to reduce their size, without sacrificing efficiency. The comprehensive review of low-profile VGs by Lin (2002) shows that small ($h/\delta \sim 0.2$) VGs are just as effective in preventing separation as the normal-sized ($h/\delta \sim 1$) devices. It was concluded that low-profile VGs should be applied when the detachment point is relatively fixed, and the VGs can be positioned close to the separated region. Yao, Lin & Allan (2002) used stereoscopic particle image velocimetry (PIV) to compare a low-profile VG ($h/\delta = 0.2$) with a conventional one. In that study it was shown that the maximum vorticity generated increases as the angle of attack increases, from 10°, for the small VG, but it decreases with angle of attack for the large VG due to stall. Apart from this result there are no fundamental differences between the two VGs.

Godard & Stanislas (2006) made an optimization study of co- and counter-rotating VGs submerged in the boundary layer. They concluded that triangular blades are better than rectangular blades, both in terms of vortex strength and drag. They also found that the counter-rotating set-up is twice as effective as the co-rotating in increasing the wall shear stress and that the optimum angle of attack is about 18°.

In another recent experiment Angele & Muhammad-Klingmann (2005) made extensive PIV measurements to show the flow and vortex development inside a turbulent boundary layer with a weak separation bubble. The bubble was controlled by VG arrays with different sizes (but all with $h < \delta$). They concluded that the important parameter with respect to the efficiency of the VG is the circulation of the

streamwise vortices. Although the circulation of the vortex may be hard to determine experimentally they found that it scales with the height of the generator blade and the velocity at its upper edge. Lögdberg (2006) later confirmed their findings and also showed that the separation is avoided altogether after only a small increase in circulation.

1.3. *Layout of the paper*

The present study complements earlier studies with embedded VGs in ZPG boundary layers through extensive hot-wire mapping of the flow field, for both VGs giving a pair of counter-rotating vortices and arrays of VGs. The flow behind yawed VGs, with respect to the base flow, was also investigated. An extended vortex model taking viscous effects into account was shown to give good agreement with the measured vortex motion.

Section 2 describes the wind tunnel set-up, the measurement technique and the VG family used. In § 3 the results regarding the downstream vortex development are given, and in § 4 results with yawed VGs with respect to the base flow are shown. The extended model for the vortex development is presented in § 5, and the paper ends with conclusions in § 6.

2. Experimental set-up and flow condition

In this section the experimental set-up in the MTL (minimum turbulence level or Mårten Theodore Landahl, after its initiator) wind tunnel is presented together with the VGs that were used and the techniques for flow visualization as well as velocity measurements. The section also treats the characterization of the base flow, i.e. a ZPG turbulent boundary layer, in which the streamwise evolution of vortices have been studied.

2.1. *Wind tunnel*

The experimental investigation of the streamwise evolution of longitudinal vortices was carried out in the MTL wind tunnel, which is located at KTH Mechanics in Stockholm. This wind tunnel is of closed-circuit type and was designed with the aim to have a low background disturbance level. At the nominal velocity of $U_0 = 25\,\mathrm{m\,s^{-1}}$ the high pass filtered root mean square velocity values are less than 0.025 %, 0.035 % and 0.035 % of the free stream velocity in the streamwise, wall-normal and spanwise directions, respectively. The applied cutoff frequency was defined as $f_c = U_0/\lambda_s$, where λ_s is the sum of the two test-section side lengths, assuring that all disturbances with wavelengths fitting in the cross-sectional area are conserved. The air temperature can be regulated within $\pm 0.05\,^{\circ}\mathrm{C}$ by means of a heat exchanger, which is located just upstream of the first corner after the axial fan (DC 85 kW). At the nominal velocity the total pressure variation is less than ± 0.06 %. For further information regarding the flow quality in the MTL wind tunnel the interested reader is referred to Lindgren & Johansson (2002).

The test section is 7.0 m long and has a cross-sectional area of 1.2 m × 0.8 m (width × height). A horizontal 5.8 m long flat plate, which spans the whole width of the test section, was mounted with its upper surface 0.51 m from the test section ceiling at the leading edge. The ceiling is adjustable in order to make compensating for the boundary layer growth possible and was here adjusted to give a zero streamwise pressure gradient at the nominal free stream velocity. The boundary layer was tripped by means of eight rows of Dymo tape embossed with the letter 'V' at the flat plate leading edge to ensure a spanwise homogenous boundary layer transition. The

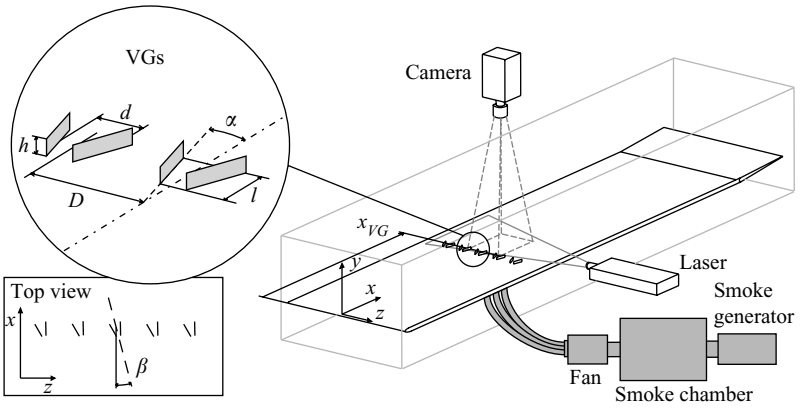

FIGURE 2. Sketch of the experimental set-up, flow visualization arrangement and VG geometry.

plate was waxed to make it smooth, but no measurement of the surface roughness was performed, since this parameter was considered insignificant in this particular experiment.

A sketch of the experimental set-up is shown in figure 2. The coordinate system is chosen with the origin at the leading edge centreline of the plate, and the coordinates x, y and z correspond to the streamwise, wall-normal and spanwise directions, respectively.

The MTL wind tunnel is equipped with five degrees of freedom (x, y, z and two angles α, φ) traversing system operated with computer-controlled DC motors. This together with the feature of computer-controlled wind tunnel speed allow for fully automatic *in situ* X-probe calibration (§ 2.3). In the present set-up the probe was traversable in the following measurement volume: $200 \lesssim x \lesssim 5300$, $0 \leqslant y \leqslant 130$ and $-72.5 \leqslant z \leqslant 72.5$ (mm).

2.2. *Flow visualization technique*

The near flow development behind a spanwise pair and array of vortices was first investigated through smoke visualization. The smoke was obtained by heating a glycol-based liquid with a disco smoke generator (JEM ZR20 Mk II) and then led through ventilation tubing to a stagnation chamber (80 litre in volume). Two small DC-regulated fans (12 V) were used to drive the smoke from the stagnation chamber to the 1 mm slot (205 mm in the spanwise extent) in the plate through five vinyl hoses, creating a steady leakage of smoke through the slot. The smoke was illuminated by a laser sheet, approximately 2.5 mm thick, using a continuous Argon-ion laser (LEXEL 95–4) with a laser beam of 1.5 W and a cylindrical lens. The sheet was adjusted parallel to the plate, spanning the region 3.0 mm $< y <$ 5.5 mm. At each visualized configuration 300 images were captured through the traversing system slit in the test-section ceiling with a CCD camera (1280 pixels $\times$ 1024 pixels). The image size in the physical x–z plane was $205 \times 102\,\mathrm{mm}^2$ (cf. figure 2).

2.3. *Measurement technique*

The velocity measurements were performed using hot-wire probes manufactured in-house with the anemometer operating in constant-temperature mode. Both a single-wire probe and X-probes were used for the measurements and were made

from 5.0 μm platinum wire with about 1 mm between the prongs. The probes were calibrated *in situ*, far outside the boundary layer, against a Prandtl tube. For the single-wire probe a modified King's law calibration function was used (cf. Johansson & Alfredsson 1982), and for the X-probe an angle calibration (–40° to +40°) was performed in the velocity range 7–28 m s^{-1}. A surface fit, in the least squares sense, was applied to the data and used as a transfer function (see e.g. Österlund 1999). All three velocity components (U, V, W) could be measured through double grid-point traverse by using two boundary layer X-probes, one oriented for $U - V$ and the other for $U - W$.

In the single-wire probe case the wall position was determined by decreasing the speed until a laminar boundary layer was achieved. Six wall-normal traverses, close to the wall, measuring the mean velocity in each position were used to linearly extrapolate the velocity down to zero, in that way determining the position of the wall with an estimated accuracy of 0.02 mm. In the case of the X-probe measurements the probe was photographed next to a precision manufactured 777 ± 1 μm long cylinder, and then the wall distance was determined by measuring the probe position relative to the top of the cylinder on the photograph. With this method the wall position, relative the vertical centre of the probe, was determined with an estimated accuracy of 0.01 mm.

Normally seven y–z planes were measured downstream of each test configuration. In each measurement plane there were either 266 (19×14) or 322 (23×14) grid points. The traversing and collection of data were automatic and took approximately 14 hours for seven planes. Before every 14 hour run the calibration was checked against the wind tunnel Prandtl tube. Usually a new calibration had to be performed after two runs of seven planes.

The velocity data from an X-wire probe in a gradient perpendicular to the wires need to be corrected because the simplifying assumption of uniform velocity in the probe measurement volume is not fully valid. In this experiment the worst case appears when the probe is oriented to measure the U and W velocity components in the boundary layer. In this case the wires are at different y positions that causes the wire-normal velocities and hence the cooling velocities to differ considerably. Normally this does not produce any significant error in the U component which is proportional to $E_1 + E_2$ (i.e. the sum of the voltages from wires 1 and 2) and thus a function of the mean cooling velocity in the measurement volume. The wall-normal/spanwise velocity component (V/W), on the other hand, is proportional to $E_1 - E_2$. This means that any velocity gradient in z/y will produce an erroneously measured velocity in V/W. In the experiments reported here the data are corrected using the procedure described by Cutler & Bradshaw (1991). Only the mean velocity components V and W and the covariances $\langle uv \rangle$ and $\langle uw \rangle$ are corrected. In U the error is very small, and the correction terms of the velocity variances $\langle u^2 \rangle$, $\langle v^2 \rangle$ and $\langle w^2 \rangle$ include terms not known from the measurements.

In figure 3 mean velocity profiles for different Reynolds numbers are shown for both single-wire (seven Reynolds numbers) and X-wire probes (three Reynolds numbers). The figure has been cut at about $y^+ = 80$ in order to emphasize the comparison between the two probes. In order to assess an estimated error of the X-probe data compared to the single-wire data the standard deviations of the mean and root mean square values of the X-probe values as compared to the single-wire data, normalized by the respective maxima, were calculated. The results are (0.0011, 0.0012, 0.0014) and (0.0086, 0.0097, 0.0087) for the three Reynolds numbers in exceeding order, for the mean and root mean square standard deviations, respectively. This means that

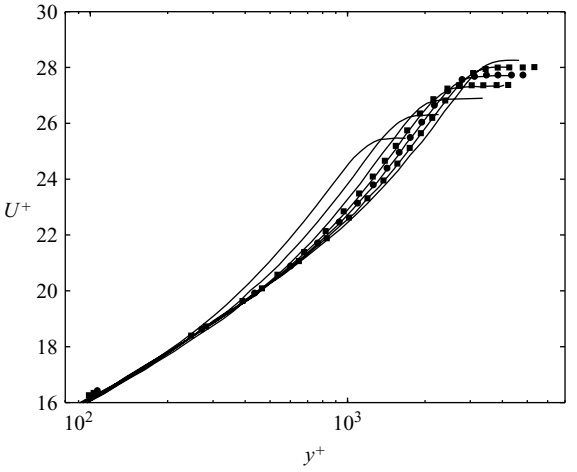

FIGURE 3. Mean streamwise velocity profiles in inner-law scaling for $Re = 3670$, 5100, 6370, 7540, 8710, 9780 and 10770 in the present ZPG turbulent boundary layer. Solid lines correspond to single-wire probe data and symbols to X-wire probe data, corresponding to $Re = 7540$, 8710 and 9780.

the mean values are measured within 0.2 % of accuracy, and the root mean square values are measured within 1 % of accuracy with the applied sampling time.

2.4. *ZPG base flow*

In this subsection it is shown that the present turbulent boundary layer that develops on the flat plate in the MTL wind tunnel has the characteristics that are typical of a ZPG turbulent boundary layer. For these measurements a single-wire probe was used (cf. § 2.3).

At all velocity measurements the free stream velocity U_∞ was set to $26.5\,\mathrm{m\,s^{-1}}$, and the temperature was kept constant at 18.1° C. The variation of the free stream velocity was measured by traversing the probe along the test-section centreline at $y =$ 120 mm. The test-section ceiling was adjusted to give a velocity variation of less than 0.5 %.

Wall-normal velocity profile measurements were performed at nine different streamwise positions from $x = 500$ mm to $x = 4500$ mm. According to Österlund (1999) the boundary layer is fully developed, in the sense that there exists a significant logarithmic overlap region, when the Reynolds number Re based on the momentum thickness (δ_2) is larger than 6000, and at $Re \gtrsim 7000$ even the second-order moment of the pressure seems to be fully developed in a turbulent boundary layer (see Tsuji *et al.* 2007). In the present experiment Re reaches a value of 6000 a small distance upstream of $x = 2000$ mm.

The skin friction was not measured independently but calculated from Re using the equation

$$c_f = 2\left[\frac{1}{\kappa}\ln(Re) + C\right]^{-2}, \tag{2.1}$$

which is derived from the logarithmic skin friction law. Österlund *et al.* (2000) fitted this relation to a large set of data obtained using oil-film and near-wall methods in the MTL wind tunnel. The values of the constants reported by Österlund *et al.* (2000) in this way are $\kappa = 0.384$, $C = 4.08$. When the skin friction is known the friction velocity

x (mm)	U_∞ (m s^{-1})	u_τ (m s^{-1})	$1000\,c_f$	Re	δ_1 (mm)	δ_2 (mm)	H_{12}	δ_{99} (mm)
500	26.4	1.09	3.41	2260	1.88	1.28	1.47	10.4
1000	26.4	1.04	3.09	3670	3.02	2.08	1.45	17.2
1500	26.4	1.00	2.89	5100	4.01	2.89	1.39	23.7
2000	26.4	0.98	2.77	6370	5.04	3.60	1.40	29.9
2500	26.4	0.97	2.68	7540	5.97	4.26	1.40	35.9
3000	26.5	0.96	2.61	8710	6.78	4.90	1.38	41.6
3500	26.5	0.95	2.55	9780	7.66	5.51	1.39	47.5
4000	26.5	0.94	2.50	10770	8.63	6.07	1.42	53.2
4500	26.6	0.93	2.45	12200	9.62	6.86	1.40	60.2

TABLE 1. Description of the ZPG turbulent boundary layer. Here Re is based on δ_2.

VG	Symbol	h (mm)	d (mm)	l (mm)	D (mm)	l/h	D/h	h/δ_{99}	U_h/U_∞
VG_6	◇	6	12.5	18	50	3	8.33	0.22	0.74
VG_{10}	□	10	21	30	83	3	8.33	0.36	0.81
VG_{18}	○	18	37.5	54	150	3	8.33	0.65	0.92

TABLE 2. Physical dimensions of the VG sets used in the experiment together with some relative boundary layer measures. The last two columns are based on $U_\infty = 26.5$ m s^{-1} and $x = 1830$ mm, where $\delta_{99} = 27.8$ mm. U_h is the velocity at the tip of the VG. See figure 2 for a clarification of the parameters. Note that the subindex in VG stands for the height (h) of the VG.

can be calculated as $u_\tau = U_\infty(c_f/2)^{1/2}$. The main features of the streamwise evolution of the turbulent boundary layer are collected in table 1, and some quantities will be used for later comparison. Here, the so far non-defined boundary layer thicknesses are the displacement thickness (δ_1) and the thickness at which the velocity reaches 99 % of U_∞ (δ_{99}). The shape factor H_{12} is defined as δ_1/δ_2.

2.5. *VGs and test configurations*

In order to set up the streamwise vortices inside the turbulent boundary layer traditional square blade VGs were used (see figure 2). Three different sizes of the VGs were used and arranged as both single spanwise pairs (^{p}) and spanwise arrays (^{a}) to create counter-rotating vortices inside the boundary layer. A summary of the dimensions and relative boundary layer measures are found in table 2. The blade angle α was kept at 15°, and the design followed the criteria suggested by Pearcy (1961) for persistent streamwise existence of the vortices. The different VG sizes were geometrically 'self-similar'.

The spanwise extension of the arrays was between 660 mm and 750 mm; thus, they did not span the whole width of the test section, only 55 %–63 %. For the 6 mm, 10 mm and 18 mm arrays (VG_6^a, VG_{10}^a, VG_{18}^a) 13, 9 and 5 VGs were used, respectively. The vortex generators were mounted with the trailing edge of the blades at $x_{VG} = 1830$ mm, where the boundary layer had reached an Re of approximately 6000 at the prescribed free stream velocity. This was to ensure a fully developed turbulent boundary layer and thus avoid any peculiarities from the transition process.

The VG_{10}, in both pair and array, was also tested varying the yaw angle β between 0° to 20° with an increment of 5°. In these experiments the yawing was performed on the individual VG pair, resulting in the VG tips in an array configuration being

		x position of y–z planes (m)							
Vortex generator	β (°)	0.06	0.17	0.42	0.67	1.17	1.67	2.67	Comment
VG_6^p	0	×	×	×	×	×	×	×	–
VG_6^a	0	×	×	×	×	×	×	×	–
VG_{10}^p	0	×	×	×	×	×	×	×	–
	5	×		×		×			–
	10	×		×		×			–
	15	×		×		×			–
	20	×		×		×			–
VG_{10}^a	0	×	×	×	×	×	×	×	–
	5	×							–
	10	×		×	×	×	×	×	U and V component
	10	×							U and W component
	15	×							–
	20	×	×	×	×	×	×	×	U and V component
	20	×							U and W component
VG_{18}^p	0	×	×	×	×	×	×	×	–
VG_{18}^a	0	×	×	×	×	×	×	×	–

TABLE 3. All tested VG configurations. The x positions of the measured y–z plane correspond to the distance from the trailing edge of the VG. Unless anything else is stated all three velocity components have been measured. Note that the subindices p and a in VG stand for the 'pair' and the 'array' configuration, respectively.

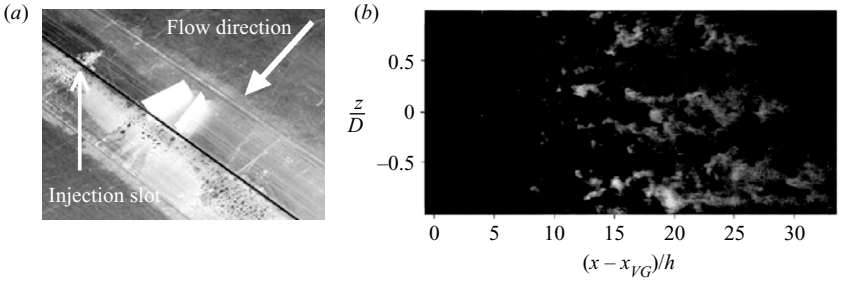

FIGURE 4. (*a*) A VG pair, VG_6^p, mounted upstream of the smoke injection slot. The flow direction is diagonal, from the upper right corner to the lower left. (*b*) An instantaneous image without VG. The smoke is injected at $(x - x_{VG})/h = 0$ but is not visible until approximately $(x - x_{VG})/h = 7$ when the smoke particles have been diffused high enough to be in the illuminated zone.

exposed to the same local velocity (U_h) (see figure 2). All tested configurations are summarized in table 3.

3. The flow field downstream of VGs: pairs vs arrays

3.1. *Smoke visualization*

The set-up for the smoke visualization is described in § 2.2 and was here used in the VG_6 configuration. Both a pair and an array of VGs were tested, which were mounted immediately upstream of the smoke slot (figure 4*a*). The free stream velocity was 25 m s^{-1}, and the camera exposure time was set to 0.10 ms for a good compromise between sensitivity and resolution. The bright vertical line, which can be seen in the

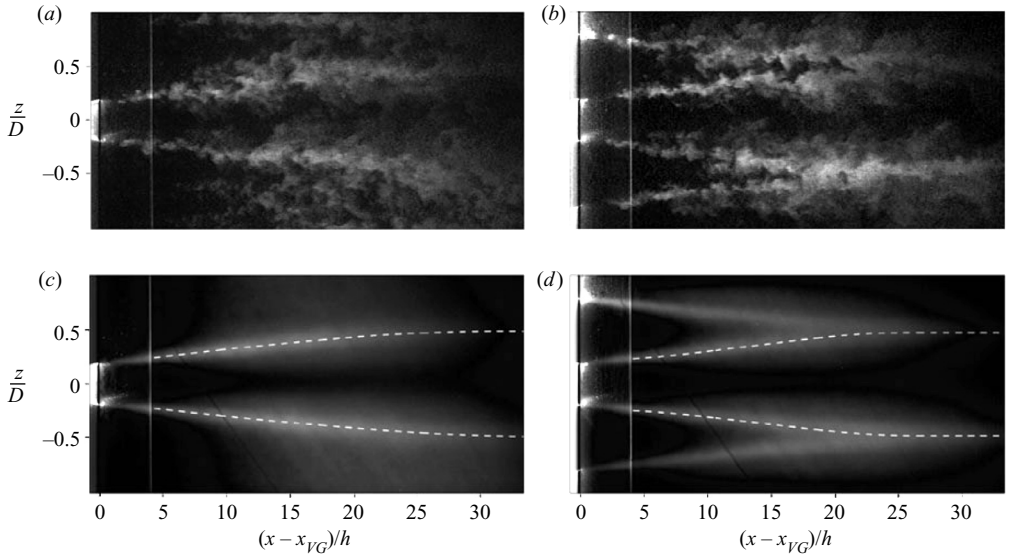

FIGURE 5. Instantaneous images at 25 m s^{-1} with the configurations (*a*) VG_6^p and (*b*) VG_6^a (*c*), (*d*) The corresponding averaged images. Dashed lines indicate the spreading of the peak in light intensity, which corresponds to the position of the maximum positive mean wall-normal velocity component.

figures 4(*b*) and 5 at $(x - x_{VG})/h$ around 4, originated from the joint between the smoke injection insert and the flat plate, and was due to reflection of light. The case without vortex generators is seen in figure 4(*b*). The lower limit of the laser sheet was at $y = 3$ mm, and it is clear from the figure that the smoke was not diffused high enough from the plate to be illuminated by the laser until $(x - x_{VG})/h$ about 7. Turbulent structures were seen in the interval $(x - x_{VG})/h = 10$–30, as would have been in a regular turbulent boundary layer.

A single image of the smoke visualization, taken of the configuration VG_6^p shown in figure 4(*a*), can be seen in figure 5(*a*). Since the smoke was lifted up to the laser sheet by the vortices, it could be seen instantly after the smoke injection slot. The vortices produced clear bands of smoke that are fairly steady from image to image. When VGs were added to the single pair to form an array, VG_6^a, the smoke bands from the neighbouring VGs seemed to converge around $(x - x_{VG})/h = 25$ (see figure 5*b*).

Figure 5(*c*,*d*) shows the result of averaging 300 images in the VG_6^p and the VG_6^a configuration, respectively. This produces images in which the light intensity indicates the averaged position of the smoke band. A least squares fit was made to the light intensity peaks of each pixel column to produce the white dashed lines. Note that the lines do not show the paths of the vortex centres. It is rather the position of the maximum positive mean velocity in V at $y = 3$–5.5 mm. Thus the vortex centre paths are located somewhere between the white lines (which will be shown in § 5).

In figure 6 the spreading of the two dashed lines from figure 5(*c*,*d*) are compared. Furthermore, the light intensity variation across the image is also shown at a number of x positions. The reduction of the peak height, with increasing x, is a combination of smoke diffusion and an increase in vortex size. Somewhat surprisingly, the lines for the VG_6^p and the VG_6^a seem to collapse, but it should be noted that in the area in which they are expected to deviate, i.e. the most downstream part of the image, the smoke density is getting lower and the results are less reliable.

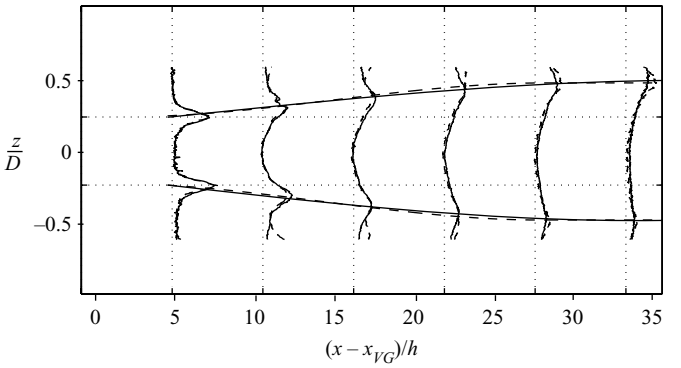

FIGURE 6. The white dashed lines from figure 5(c, d) superimposed on each other. The solid line is the VG_6^p configuration, and the dashed line is the VG_6^a. Also shown is how the light intensity varies in the spanwise direction at six x positions.

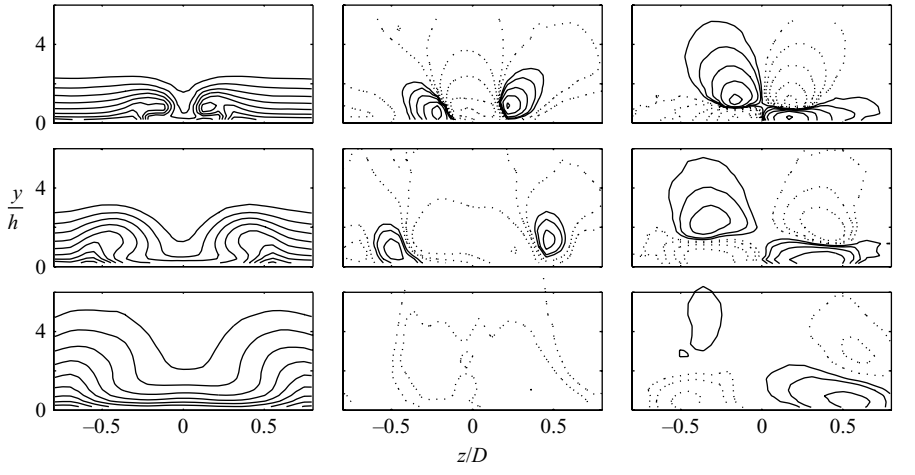

FIGURE 7. All three mean velocity components (from left to right, streamwise, wall-normal and spanwise) in the boundary layer in the VG_{10}^p configuration. From top to bottom the rows correspond to $(x - x_{VG})/h = 6$, 42 and 167, respectively. The contour levels for U/U_∞ are (0.05:0.05:0.95). For V/U_∞ the levels $[-10^{(-3/3:1/3:-7/3)}; 10^{(-7/3:1/3:-3/3)}]$, $[-10^{(-4/3:1/3:-7/3)}; 10^{(-7/3:1/3:-5/3)}]$ and $[-10^{(-5/3:1/3:-7/3)}; -]$ are plotted for the exceeding downstream positions, respectively. The corresponding contour levels for W/U_∞ are $[-10^{(-2/3:1/3:-7/3)}; 10^{(-7/3:1/3:-2/3)}]$, $[-10^{(-4/3:1/3:-7/3)}; 10^{(-7/3:1/3:-4/3)}]$ and $[-10^{(-5/3:1/3:-7/3)}; 10^{(-7/3:1/3:-5/3)}]$. Positive and negative contour levels are plotted with solid and dotted lines, respectively.

The important result from this near wake flow visualization is that there is no substantial difference in the evolution of vortices between the VG pair and array configurations at least up to $(x - x_{VG})/h$ of about 35.

3.2. *Mean flow*

The vortex generators set up strong vortices which modified the base flow. In figures 7 and 8 the three mean velocity components are the plotted contours of the VG_{10} pair and array configurations, respectively. It can be observed that even after the corrections described in § 2.3 some error in the V component is present. This is due to the difficulty in applying the appropriate correction when there are large velocity gradients in all cross-flow directions (see § 2.3 and the discussion therein). The U and

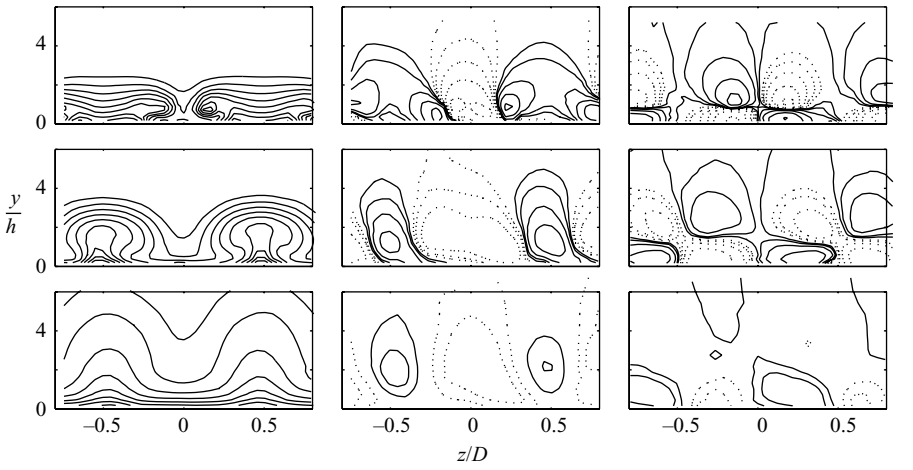

FIGURE 8. Same as in figure 7 but for the VG^a_{10} configuration. The contour levels for U/U_∞ are (0.05:0.05:0.95). For V/U_∞ the levels $[-10^{(-3/3:1/3:-7/3)};\ 10^{(-7/3:1/3:-3/3)}]$, $[-10^{(-5/3:1/3:-7/3)};\ 10^{(-7/3:1/3:-4/3)}]$ and $[-10^{(-6/3:1/3:-7/3)};\ 10^{(-7/3:1/3:-6/3)}]$ are plotted for the exceeding downstream positions, respectively. The corresponding contour levels for W/U_∞ are $[-10^{(-2/3:1/3:-7/3)};\ 10^{(-7/3:1/3:-2/3)}]$, $[-10^{(-4/3:1/3:-7/3)};\ 10^{(-7/3:1/3:-4/3)}]$ and $[-10^{(-6/3:1/3:-7/3)};\ 10^{(-7/3:1/3:-6/3)}]$. Positive and negative contour levels are plotted with solid and dotted lines, respectively.

W components are symmetric; however the asymmetry in the V component is due to the large velocity gradients which affect the cooling velocities of the two wires of the X-probe differently. The maximum magnitude of the cross-flow components are approximately 15 % of U_∞ in V and 26 % in W at $(x - x_{VG})/h = 6$ for a VG pair. For the VG array they are 13 % and 26 %, respectively. At this x position both V and W are symmetric in the sense that the negative and the positive velocities are of the same magnitude and are expected to be even larger closer to the VGs. The cross-flow components decrease with downstream distance as the vortex grows. As far downstream as $(x - x_{VG})/h = 267$ (not shown here), the ranges of V and W are however still 1.8 % and 3.2 % of U_∞ in the VG^p case and 2.3 % and 2.4 % in the VG^a case. At $(x - x_{VG})/h = 267$ the V component no longer has positive and negative velocities of the same magnitude due to the boundary layer growth. Hence, the range between the maximum and the minimum values becomes a better measure than the magnitude, when comparing with the still-symmetric W component.

The mean velocities of a VG^p case (figure 7) can be compared to that of an array in figure 8. Most noticeable is the larger symmetry in the VG^a_6 case for all three velocity components. With an array of VGs there is a small increase in the boundary layer thickness. For counter-rotating vortices the V component of the neighbouring vortices is added, and thus it persists further downstream. For W the effect of the array is the opposite, and this velocity component decays faster compared to the VG pair case. Both effects are clearly visible in the figures.

For control purposes the induced drag due to the presence of the VGs is an important factor, which has to be taken into account as a cost in any performance improvement estimation. Here, we have calculated the spanwise-averaged local skin friction (c_f) by considering the momentum loss for the array case by integrating over

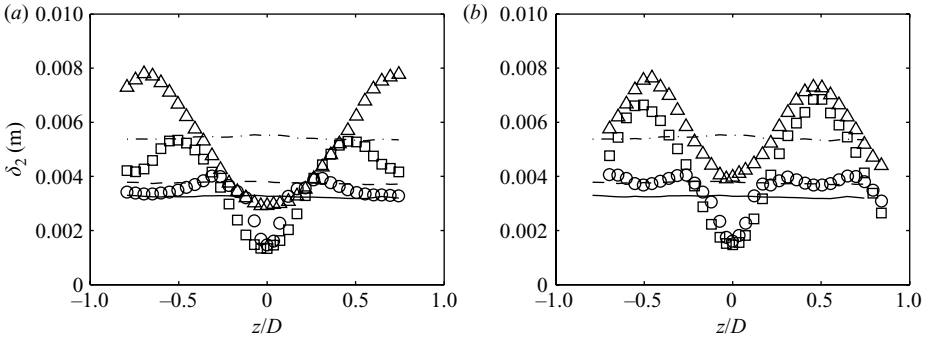

FIGURE 9. Spanwise distribution of the momentum thickness for different downstream positions with (symbols) and without (lines) VGs. (*a*) The VG^p_{10} configuration. (*b*) The VG^a_{10} configuration. The symbols and lines – ○ solid, □ dashed and △ dash-dotted – correspond to $(x - x_{VG})/h = 6$, 42 and 167, respectively.

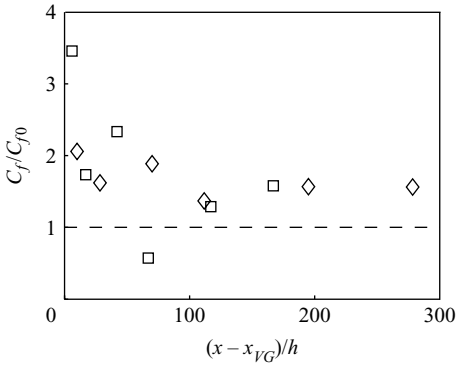

FIGURE 10. Streamwise distribution of the spanwise-averaged local skin friction coefficient (c_f). The ◇ and □ symbols correspond to VG^a_6 and VG^a_{10}, respectively. The subindex 0 denotes the case without VGs.

one spanwise period (λ) according to

$$c_f(x) = 2\frac{\tau_w}{\rho U_\infty^2}, \quad \text{with} \quad \tau_w(x) = \rho U_\infty^2 \frac{\mathrm{d}\delta_2^z(x)}{\mathrm{d}x} \quad \text{and} \quad \delta_2^z(x) = \frac{1}{\lambda}\int_{-\lambda/2}^{\lambda/2} \delta_2(x, z)\,\mathrm{d}z.$$

The streamwise derivative of the momentum thickness in the expression for $\tau(x)$ was approximated by a forward-step finite difference. In figure 9 the spanwise distribution of the momentum thickness is shown for both (*a*) the pair and (*b*) the array cases with $h = 10$ and at three different downstream positions. One may observe that the boundary layer modulation due to the VGs is different for the pair and the array cases as also concluded from figures 7 and 8. From figure 9 it is clear that the level of modulation peaks earlier, i.e. closer to the VGs, for the VG^a case compared to the VG^p case but not necessarily at a higher level. This is realized by comparing the two most downstream positions, $(x - x_{VG})/h =$ 42 and 167. Finally, in figure 10 the spanwise-averaged local skin friction is plotted versus the downstream distance for the VG^a_6 and the VG^a_{10} cases. The skin friction coefficient is normalized with the local ZPG turbulent boundary layer case without VGs, which gives a direct measure of the cost (i.e. increased drag) along the plate.

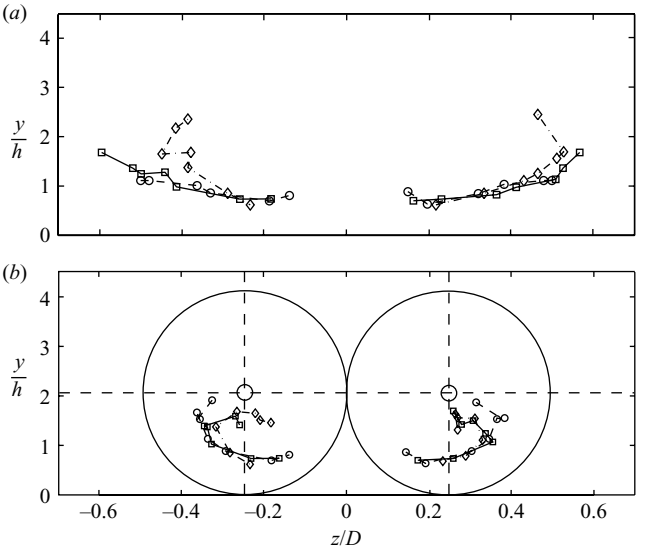

FIGURE 11. Vortex centre paths plotted in a y–z plane normal to the stream: $-\cdot\diamond\cdot-$, —□—, $--\circ--$ denote VG_6, VG_{10} and VG_{18}, respectively. (*a*) The paths downstream of a VG pair. (*b*) The same planes for an array of VGs.

3.3. *Vortex centre paths*

There exist a number of different methods for vortex indentification; for a review see Jeong & Hussain (1995). In this particular case the vortex centre is defined as the position of the maximum absolute streamwise vorticity $|\omega_x|_{max}$. This method would give the same result as the Q method proposed by Hunt, Wray & Moin (1988), i.e. by identifying the maximum positive values of the second invariant of the velocity gradient tensor denoted by Q, since the background shear in the turbulent boundary layer of the position of the vortex cores is weak compared to the vorticity magnitude within the vortex. The vortices generated by VGs are relatively strong and steady, implying that any method would work well. The second invariant Q is defined as $1/2(U_{i,i}^2 - U_{i,j}U_{j,i})$, and the streamwise component becomes

$$Q_x = -\frac{1}{2}\frac{\partial W}{\partial y}\frac{\partial V}{\partial z}, \tag{3.1}$$

to which we will come back later.

In order to determine the vortex centres a simple interpolation scheme was used. To find the vortex centres of each plane the data positions of the maximum and minimum streamwise vorticities were identified, for the positively and negatively rotating vortices respectively. Then, a cubic surface fit was applied on the surrounding 24 points (± 2 in y and z) and a new 20×20 matrix, with higher spatial resolution, was produced in which a new maximum or minimum was found. Since the peak of maximum absolute vorticity is getting flatter as the vortices are convected downstream, and the vorticity is diffused so that the area of the vortex core is increased, the position of maximum/minimum vorticity becomes more diffused. Thus the vortex centre coordinates get less precise with increasing x.

In figure 11(*a*) the vortex centre paths from VG pairs are projected on the y–z plane. The three curves do not start on the same streamwise location, since the first

data point in each case are not located at the same normalized streamwise position, $(x - x_{VG})/h$. The paths of the vortices behind the VG^p_{10} and the VG^p_{18} seem to collapse nicely over each other. Progressing downstream these vortex paths move away from each other; at first one may observe a small approach towards the wall which is followed by a steady rise until the last measured streamwise position. This can be understood using the same reasoning as Pearcy (1961), based on potential flow theory, for VG arrays. The downward motion in the beginning is caused by the induced velocity by the neighbouring real vortex, which leads to a stronger induced force away from each other due to the mirrored vortices at the plate. However, as the two vortices move away from each other the former influence becomes weaker, and the growth of the vortex causes the vortex centre to move away from the wall. An interesting behaviour of the VG^p_6 vortex path is that, after about $(x - x_{VG})/h = 200$–250, it makes an unexpected turn and starts to approach its neighbour. An explanation of this peculiarity will be given below.

The corresponding vortex paths of the VG arrays are shown in figure 11(*b*), and it is seen that they look similar to the VG^p_6 case. First they move apart and towards the wall due to the same reason as in the VG pair case. But in the case of the array, when they move away from each other they are moving closer to the vortex from the neighboring vortex pair and eventually form a new counter-rotating pair – this time with common upflow. The induced velocities in the new pair will tend to lift the vortices, and according to the inviscid theory (Jones 1957) they will continue to rise from the wall with a constant slope, along an asymptotic value of z/D in the horizontal plane. However, the measurements show that the vortex centre paths of the original pair, while still rising, start to move towards each other again. This is probably due to vortex growth; when the area of the vortex grows the vortices are forced to a spanwise equidistant state. The influence from the other vortices (real or mirrored) is decreasing with increasing downstream distance. At $(x - x_{VG})/h = 50$ the circulation is reduced to half of the initial value, and thus the induced flow is equally reduced. Since the distance between the VG pairs in an array is D, and each VG pair produces two vortices, the maximum vortex radius in an equidistant system of circular vortices is $D/4$. If the distance from the vortex centre to the wall is $D/4$, the induced velocities from the real vortices and the three closest mirrored vortices all cancel. The following mirrored vortex images will produce small, alternating positive and negative forces in the spanwise direction, and the system will be close to balanced. In these experiments $D/h = 8.33$ (cf. table 2), and thus $D/4 = 2.08h$. Hence, if the assumption holds, the vortex centres should approach $(y/h,\ z/D) = (2.08, \pm 0.25)$. In figure 11(*b*), these coordinates are marked with small circles, whereas the large circles show the maximum size of a circular spanwise equidistant vortex. There seems to be a tendency for the vortex centres to move towards the predicted position.

Now, one can understand the peculiar vortex centre path produced by the VG^p_6 in figure 11(*a*). Analogous to the paths of the vortices generated by the array, the curving back motion appears to indicate the existence of more vortices, outside of the primary pair. The three most downstream planes, $(x - x_{VG})/h = \{194,\ 278,\ 445\}$, certainly show two more vortices flanking the original ones. The new induced secondary vortices are relatively strong; at $(x - x_{VG})/h = 194$ their circulation is about 25 % of the primary vortices, and at $(x - x_{VG})/h = 278$ they have reached a strength close to 50 %. At $(x - x_{VG})/h = 445$ a small part of the secondary vortices is outside the measurement plane, but the major part is inside, and the circulation is about 55 % of the primary vortices. Note that the circulation of the primary vortices has ceased to decay in this region and that the secondary vortices thus not only increase in

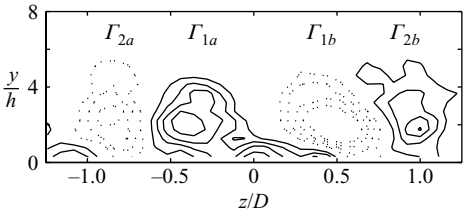

FIGURE 12. Contours of $\omega_x/(U_\infty/h)$ in the y–z plane at $(x - x_{VG})/h = 278$, downstream of a 6 mm VG pair; Γ_1 and Γ_2 denote the circulation of the primary and secondary (induced) vortices. The solid lines indicate positive vorticity with contour levels $(2.5 : 2.5 : 10) \times 10^{-3}$ and the dashed lines negative vorticity with contour levels $(-10 : 2.5 : -2.5) \times 10^{-3}$.

strength relative to the primary vortex pair but also grow in absolute numbers. Partly this is due to their increasing distance from the wall, moving more of the secondary vortices into the measurement plane, but the major increase in circulation is due the continuous vorticity transfer from the primary vortices close to the wall to the upwash regions. In figure 12, the plotted vorticity contours reveal the existence of an outboard pair of induced secondary vortices at $(x - x_{VG})/h = 278$.

The secondary vortices originate from the very thin layer of stress-induced opposing ω_x under the primary vortex. This layer is too thin to be detected in the experiments reported here but is described in Shabaka *et al.* (1985). According to Pauley & Eaton (1988) there is some evidence that the layer of opposing vorticity is convected out to form a small low-momentum region of opposing vorticity on the upflow side of the main vortex and close to the wall. To the authors knowledge it has never been shown before how this induced vorticity is rolled up into a vortex that rises up from the wall to influence the vortex centre path of the primary vortex.

In figure 13(*a*) the vortex paths from the single VG pair are shown in plan view. The paths from the VG_6^p continue to $(x - x_{VG})/h = 445$, but in order not to compromise the resolution the figure is cut at $(x - x_{VG})/h = 300$. This also applies to figures 13(*b*) and 14. A divergence of the paths, from all VG sizes, caused by the mirrored images can be observed. The angle of divergence seems to increase with vortex strength.

Vortex centre paths downstream of VG arrays are plotted in figure 13(*b*). These paths scale better than the VG^p paths, using D in the spanwise and h in the streamwise directions. In plan view it is easy to see how the paths first move apart, roughly at the same rate as in the case of the single pairs, up to about $(x - x_{VG})/h = 50$ and then how they converge towards the asymptotic spanwise location of $z/D = \pm 0.25$ as discussed earlier.

Shabaka *et al.* (1985) suggested that since turbulence diffuses both the boundary layer and the vorticity the proportion between vortex size and boundary layer thickness should remain constant at all x stations for isolated vortices in a boundary layer. For a circular vortex, this implies a vortex centre that moves away from the wall with the increase of the boundary layer thickness. According to the inviscid analysis by Jones (1957) the interaction of the vortex pairs will make them move away from the wall linearly after an initial approach towards the wall. Earlier in this section it was suggested that the vortex centres will move towards a constant height $y = D/4$. In figure 14 the vortex centre paths are plotted on a plane parallel to the stream. These paths seem to scale with h, and in the figure the boundary layer thicknesses (δ_{99}) for the different VG sizes are also plotted. It is clear from the figure that the vortex centre height does not scale with the boundary layer thickness regardless of

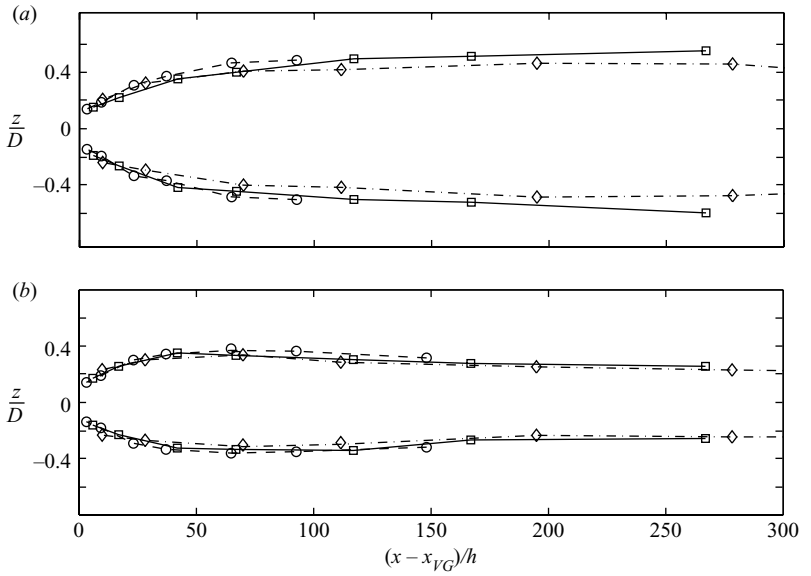

FIGURE 13. Vortex centre paths plotted in plan view (the x–z plane): — · ◇ · —, —□—, — — ○ — — denote $h_{VG} = 6$ mm, 10 mm and 18 mm. (*a*) The paths downstream of a pair of vortex generators. (*b*) The same planes for a VG array. Note that for the array the paths of the neighbouring vortices are actually within the figure area, but for the sake of clarity they are not shown.

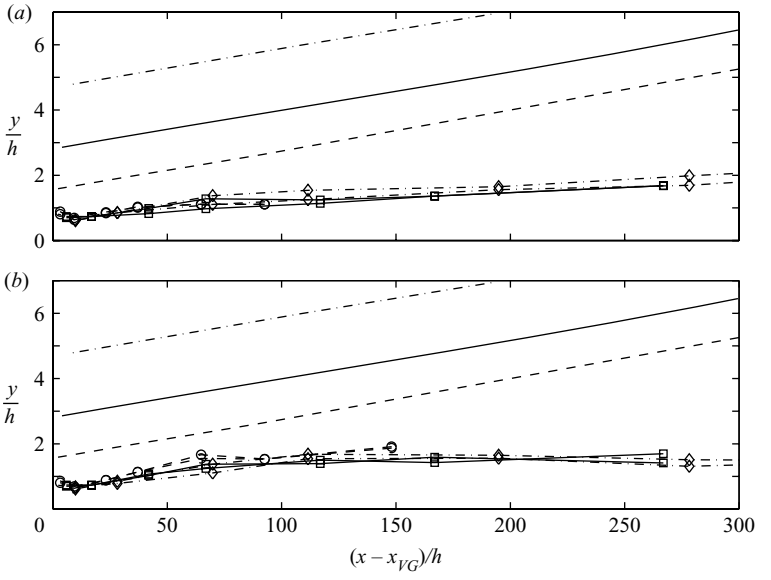

FIGURE 14. Vortex centre paths plotted in a plane parallel to the stream (the x–y plane): — · ◇ · —, —□—, — — ○ — — denote $h_{VG} = 6$ mm, 10 mm and 18 mm. (*a*) The paths downstream of a pair of vortex generators. (*b*) The same planes for a VG array. The dash-dotted line shows the boundary layer thickness in the 6 mm case; the solid line is the 10 mm case; and the dashed line is the 18 mm case. Note that the scale of the y-axis is more than 10 times that of the x-axis.

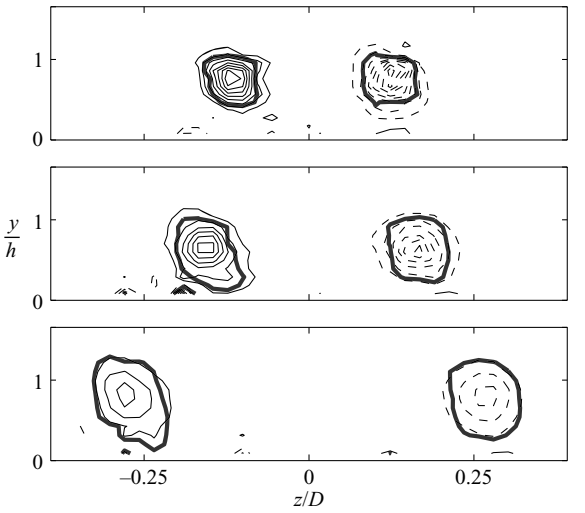

FIGURE 15. Contours of $\omega_x/(U_\infty/h)$ in the first three planes behind the VG^p_{18} configuation. The dashed and solid contour levels correspond to $(-1.8 : 0.2 : -0.2)$ and $(0.2 : 0.2 : 1.8)$, respectively. The thick contour line represents $Q_x = 0.05\, Q_x^{max}$ and encompasses the vortex core area A.

configuration. The paths seem to scale with h. The single pairs in figure 14(a) continue to rise through the test section, but the corresponding array centres in figure 14(b) seem to reach a constant height of $y/h = 1.5$–2. This range is close to the asymptotic value of $y/h = 2.08$ from the hypothesis of asymptotic path values stated above. When the wall-normal positions of the vortex centres are closer to the wall than $D/4$ the induced velocities from the mirrored images produce a force towards the neighbouring vortices with a common outflow. However the paths in figure 11(b) and 13(b) show no tendency to diverge. Thus there must be an opposing force.

3.4. *Vortex strength decay*

According to Kelvin's circulation theorem the circulation around a closed material circuit in an inviscid fluid is conserved. Thus the circulation would remain constant as the vortices are convected downstream from the VGs. In the present experiment the no-slip condition at the wall generates a spanwise shear stress component that reduces the angular momentum, and hence the circulation, of the vortex.

The vortex circulation is calculated by integrating the streamwise vorticity over the area A according to

$$\Gamma = \int_A \omega_x \, \mathrm{d}A, \tag{3.2}$$

where A is defined as the area enclosed by the contour $Q_x = 0.05\, Q_x^{max}$ (cf. (3.1)). Note that Q_x^{max} refers to the local maxima in the measured plane. The choice of cutoff level was chosen after some consistency tests. Figure 15 shows the evolution of the vortex areas of three measurement planes. Since the aspect ratio and the angle of attack are the same for all three VG sizes it is appropriate to normalize the circulation by the height h and the streamwise velocity at the blade tip U_h.

In figure 16(a,b) the downstream development of circulation for the 6 mm, 10 mm and 18 mm VGs are shown for the pair and the array cases, respectively. Here, the clearly identified asymptotic value in a linear plotting has been subtracted from the

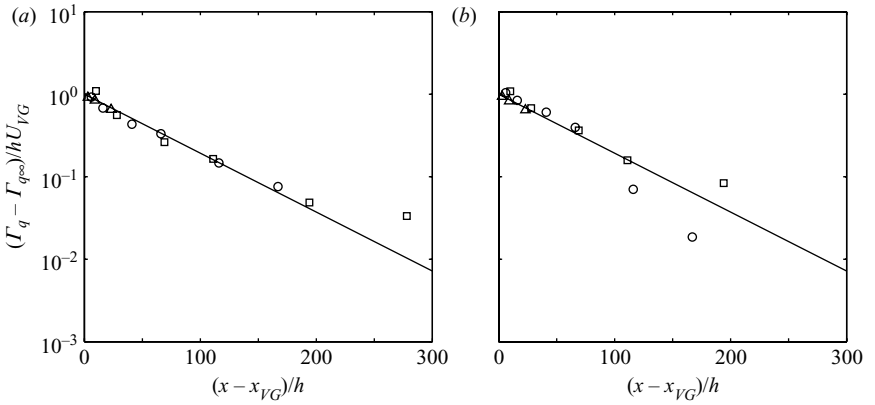

FIGURE 16. The vortex strength decay of the (*a*) VG^p and (*b*) VG^a cases. For symbols see table 2. The solid lines correspond to the exponential decay exponent −0.0164.

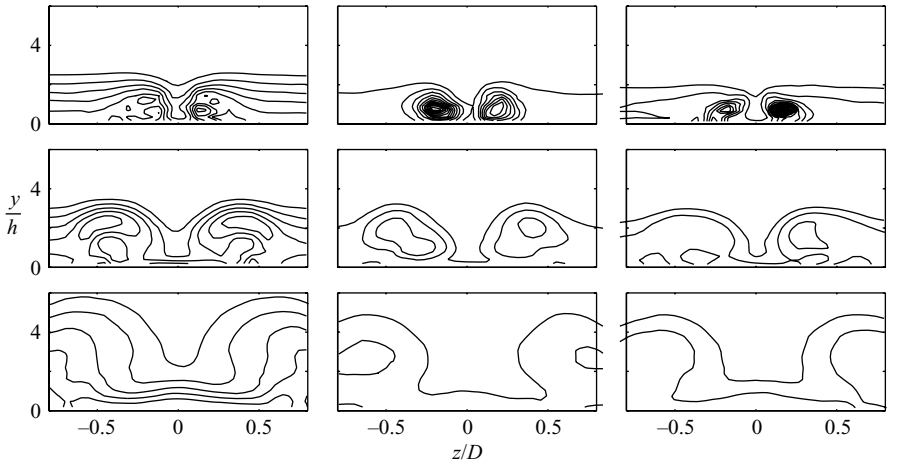

FIGURE 17. Contours of all three velocity variance components. From left to right, $\langle u^2\rangle/U_\infty^2$, $\langle v^2\rangle/U_\infty^2$ and $\langle w^2\rangle/U_\infty^2$, in the boundary layer for the VG$^p_{10}$ configuration. From top to bottom the rows correspond to $(x - x_{VG})/h = 6$, 42 and 167, respectively. The contour levels are $(1:1:8)\times 10^{-3}$ for $\langle u^2\rangle$ and $(1:0.5:8)\times 10^{-3}$ for $\langle v^2\rangle$ and $\langle w^2\rangle$.

data. In (*a*) the three curves collapse well, and down to $(x - x_{VG})/h \approx 200$ the circulation seems to decay exponentially. The same exponential decay is achieved with VG arrays, at least up to $(x - x_{VG})/h \approx 100$, as can be seen in (*b*).

3.5. *Turbulence quantities*

In this section the velocity variances and covariances of the accessible components from the two X-probes are shown for the VG_10^p and VG_10^a cases. It may be observed from figures 17 and 18, which show all three velocity variance components for the pair and array configuration, respectively, that the maxima of $\langle v^2\rangle/U_\infty^2$ and $\langle w^2\rangle/U_\infty^2$ follow the location of the strongest velocity shear of their respective mean velocity components. The streamwise velocity variance component is the largest of the three for both the pair and the array configurations with a value just below 15×10^{-3} close to the VGs when normalized with U_∞^2. However, the high fluctuation level decays

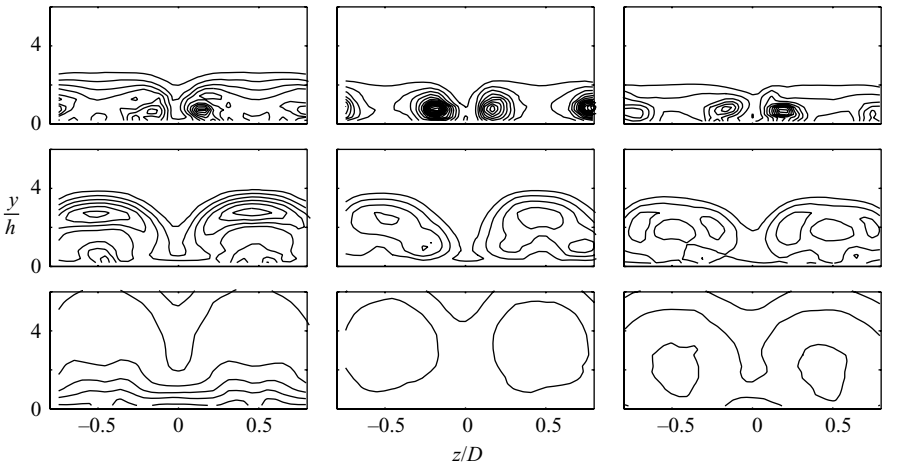

FIGURE 18. Same as in figure 17 but for the VG^{a}_{10} configuration. The contour levels are $(1:1:10)\times10^{-3}$ for $\langle u^2\rangle$ and $(1:0.5:10)\times10^{-3}$ for $\langle v^2\rangle$ and $\langle w^2\rangle$.

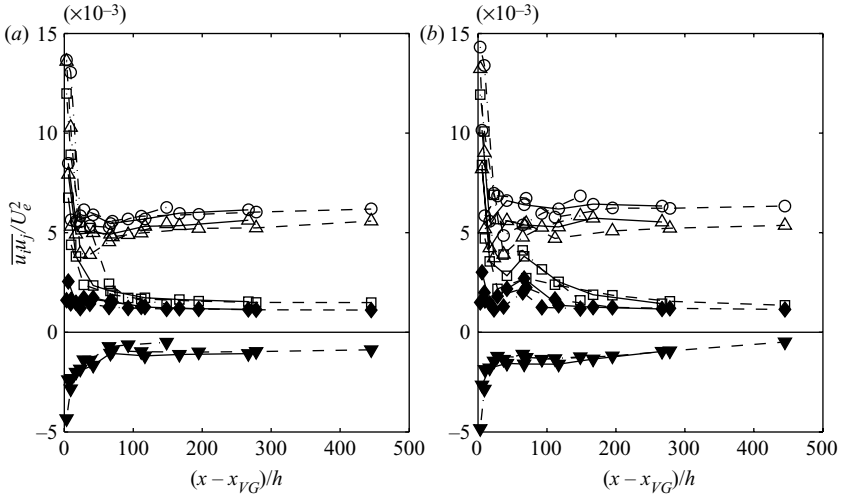

FIGURE 19. Streamwise evolution of the maximum values of the turbulence quantities shown in figures 17–21 but for all VG heights. (*a*) correspond to the pair configuration. (*b*) The array configuration. The symbols ○, □, △, ◆, ▼ correspond to $\max_{yz}\{\langle u^2\rangle/U_\infty^2,\ \langle v^2\rangle/U_\infty^2,\ \langle w^2\rangle/U_\infty^2,\ -\langle uv\rangle/U_\infty^2,\ -\langle uw\rangle/U_\infty^2\}$, respectively.

close to the VGs and reaches a constant level of $\langle u^2\rangle/U_\infty^2$ around 6×10^{-3} from about $(x-x_0)/h=150$ and beyond. In figure 19 the streamwise evolution of the turbulence quantities are plotted, and an undershoot of the decay may be observed with the minima for all three velocity variance components around $(x-x_0)/h=40$. This undershoot is the strongest for the spanwise component, which behaves as the streamwise component but shifts somewhat to a lower fluctuation level. The undershoot is an artefact of the second outer maximum in the y–z plane of all three velocity variance components, which is well developed around $(x-x_{VG})/h=42$ (cf. figures 17 and 18). A shift from the inner peak to the outer peak being the largest

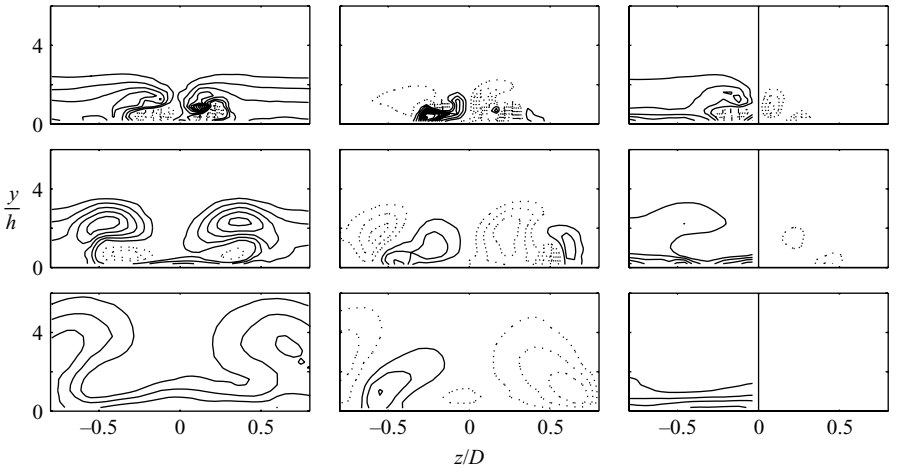

FIGURE 20. Contours of the two velocity covariances with the streamwise component and the mean streamwise velocity gradients in the cross-plane for the VG^{p}_{10} configuration. From left to right $-\langle uv\rangle/U_\infty^2$, $-\langle uw\rangle/U_\infty^2$ and $(\partial U/\partial y,\ \partial U/\partial z)\cdot\tilde{\delta}_{99}/U_\infty =$ (left, right). From top to bottom the rows correspond to $(x - x_{VG})/h = 6$, 42 and 167, respectively. The contour levels are $(-2.4 : 0.3 : 2.7) \times 10^{-3}$ and $(-1.25 : 0.25 : -0.25;\ 0.25 : 0.25 : 1.25)$ for the covariances and the gradients, respectively. Note that for the former levels the solid and dotted lines correspond to negative and positive covariances, respectively. The opposite holds for the latter levels of the gradients; $\tilde{\delta}_{99}$ is the spanwise-averaged boundary layer thickness.

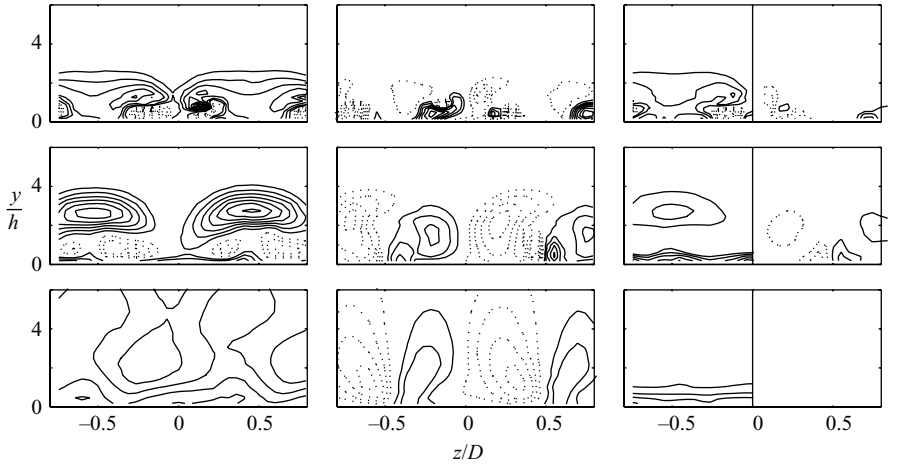

FIGURE 21. Same as in figure 20 but for the VG^{a}_{10} configuration. The contour levels are $(-2.1 : 0.3 : 2.7) \times 10^{-3}$ and $(-1.25 : 0.25 : -0.25;\ 0.25 : 0.25 : 1.25)$ for the covariances and the gradients, respectively.

gives rise to the undershoot. Similar explanation applies for the observed undershoot of the $-\langle uv\rangle$ covariance component, which however is not revealed in figures 20 and 21. On the other hand at $(x - x_{VG})/h = 17$ (not shown here) there are two clear negative outer peaks of $\langle uv\rangle/U_\infty^2$, which merge downstream, and at $(x - x_{VG})/h = 42$ only a single outer peak is observed (cf. figures 20 and 21). Worth mentioning is that the wall-normal velocity variance component is only 25 % of the others after the initial decay.

Furthermore, the larger term of the streamwise production of turbulence is $-\langle uv\rangle \partial U/\partial y$ as compared to the $-\langle uw\rangle \partial U/\partial z$ term. From figure 19 it is observed that the maxima in $-\langle uv\rangle$ and $-\langle uw\rangle$ are of opposite signs but 'equal' magnitudes. The regions of the covariance maxima and their corresponding velocity gradient maxima (cf. figures 20 and 21) appear to coincide in the cross-flow plane. The gradient $\partial U/\partial z$ has its maximum at the centre of the vortex and is zero at the outflow and inflow positions with a corresponding minimum and maximum in U, respectively, where it also changes signs. On the other hand the gradient $\partial U/\partial y$ has its maximum at the position of maximum outflow due to the S-shaped wall-normal velocity profile in U (see e.g. Angele & Muhammad-Klingmann 2005). Thus, this gives the maximum production at the position of outflow and at the centre of the vortex, corresponding to $-\langle uv\rangle \partial U/\partial y$ and $-\langle uw\rangle \partial U/\partial z$, respectively.

Finally, it is striking how well all the turbulence quantities in figure 19 scale with the VG heigth, h. Note that here all three VG heights have been plotted. The above-discussed undershoot appears around $(x - x_{VG})/h = 42$, independent of the studied turbulence quantity and despite the factor of 'three' in VG height difference between the lowest and the highest VGs.

4. The flow field downstream of yawed VGs

In many practical applications, especially ground vehicles, the VGs operate in yaw most of the time. Therefore it is of interest to study vortex generation and decay under such non-ideal conditions. Here, the VG_{10} case was chosen in both pair and array configurations (cf. table 3) for the yaw study. Yawing an array can be done in at least two different ways – either by yawing the whole array as one unit or by yawing the individual VG pairs (see the squared insert in figure 2). In this fundamental experiment the VG pairs are yawed individually in order to have the same boundary layer thickness at all blades and thus produce the same circulation for all VGs. The tested yaw angles were $0°$, $5°$, $10°$, $15°$ and $20°$. They were chosen to be relevant for flow control on ground vehicles, such as trucks. Since the blade angle α is $\pm 15°$ the 'positive' blade will be yawed to $15°$, $20°$, $25°$, $30°$ and $35°$ and the 'negative' blade to $-15°$, $-10°$, $-5°$, $0°$ and $5°$, implying that the negative blade will be parallel to the base flow in one configuration.

The purpose of introducing VGs in a flow is to increase the momentum near the wall, and in figure 22 the effect of changing the yaw angle is illustrated. Here the original ZPG boundary layer, without any vortices, is compared to the boundary layer modified by the the vortices from an array of VGs at $0°$, $10°$ and $20°$ yaw. In the upper part of the boundary layer ($y = \delta_{95}$), unless too close the VGs, the VGs slow down the fluid and make the boundary layer thicker. This is more prominent in the downstream planes. Closer to the wall ($y = \delta_{80}$) the vortices produce the desired velocity increase compared to the undisturbed ZPG case. The size of the area between the dotted and the solid black lines gives a visual indication of the momentum increase caused by the vortices. This area is almost constant for each x position, i.e. independent of the yaw angle, except for the first plane. This means that the momentum transfer to the lower part of the boundary layer neither decreases nor increases with yaw. Hence a flow control system based on the tested type of VGs will remain stable. A frequently used measure of the base flow modulation is the shape factor, which here has been calculated in order to demonstrate the overall effect of VGs in an array. Due to lack of X-probe data points near the wall, especially close to the array at the location of

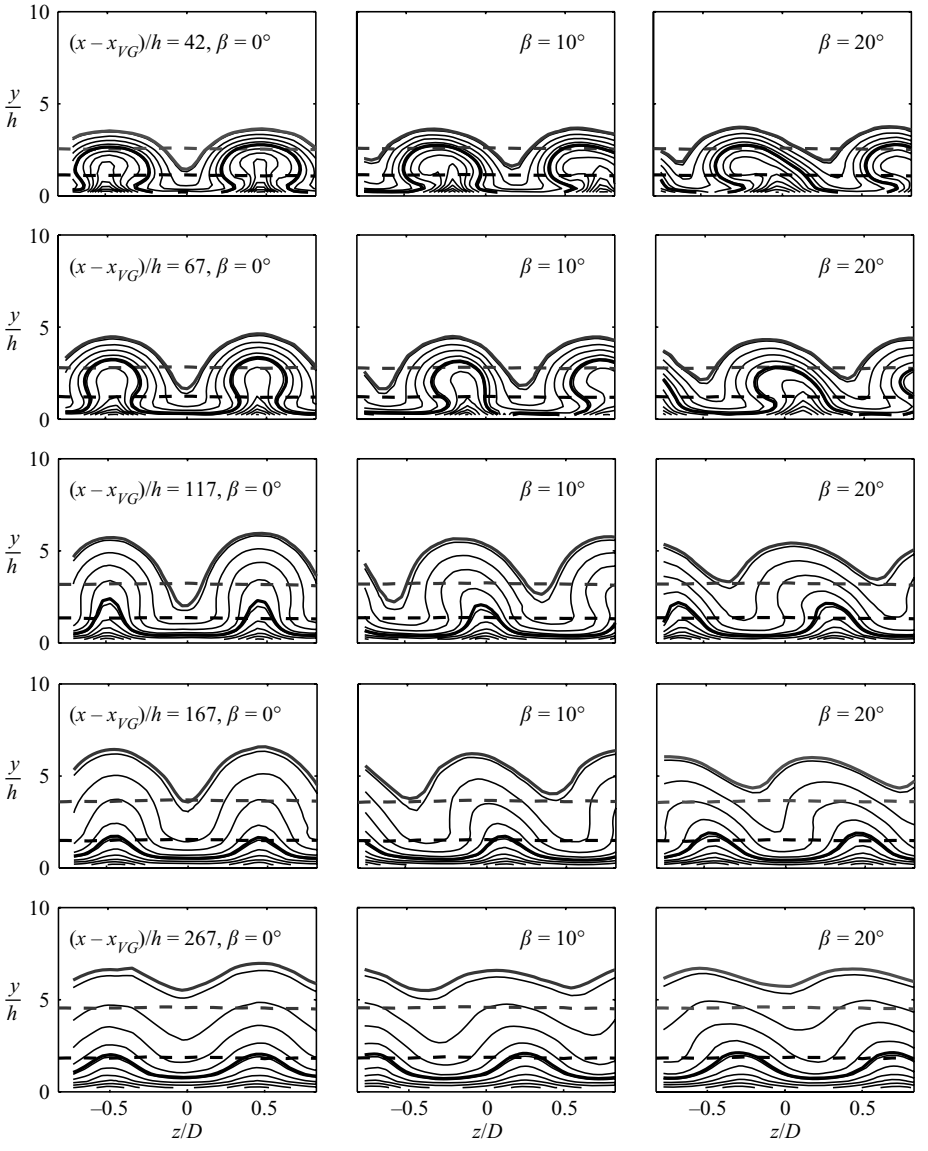

FIGURE 22. Contours of streamwise velocity at different x positions downstream of the VG^{a}_{10} case at 0°, 10° and 20° yaw. The dotted grey and black lines corresponds to $y = \delta_{95}$ and $y = \delta_{80}$ respectively, in the vortex free base flow. The bold solid grey and black lines indicate the same y positions for the shown VG cases.

strong downwash at which the boundary layer is relatively thin, the calculation of the displacement thickness gives erroneous results. To compensate for the poorly resolved near-wall velocity profiles three additional points have consistently been added to approximate the profile in this region. Apart from the point corresponding to the no-slip condition, the additional points are $y^{+} = 5$ and 50, using the law of the wall and the log law, respectively, although the spanwise variation of u_τ due to the vortices cannot be taken into account. Here it should be noted that it is not the local absolute values of H_{12} which are in focus; instead it is the spanwise-averaged values compared

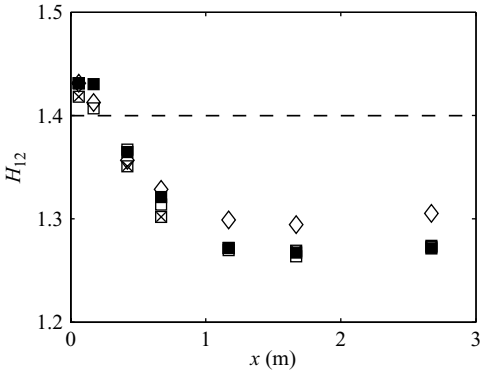

FIGURE 23. Shows the spanwise averaged shape factor for different yaw angles; □, ⊠, ■ correspond to $\beta = 0°,\ 10°,\ 20°$ for the VG^a_{10} case, respectively; ◇ corresponds to VG^a_6 at zero yaw. The dashed line represent the ZPG base flow without VGs (cf. table 1).

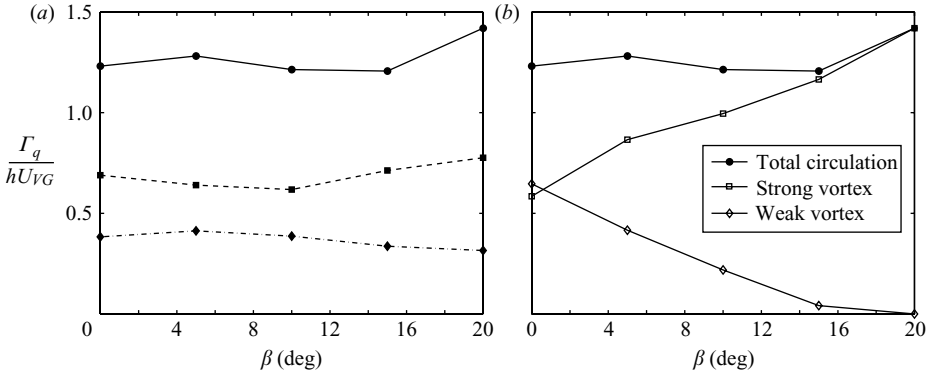

FIGURE 24. (*a*) The total circulation, i.e. the contribution from both the vortices, in the VG^p_{10} case versus the yaw angle at $(x - x_{VG})/h = 6,\ 41,\ 116$ with ○, □, ◇, respectively. (*b*) The individual contribution from the two vortices for the VG^p_{10} case at $(x - x_{VG})/h = 6$.

between the different configurations. In figure 23 the streamwise distribution of the spanwise-averaged shape factor is plotted for different yaw angles for the configuration VG^a_{10}. In addition, the natural setting ($\beta = 0$) for VG^a_6 is also compared. It is seen that close to the VG array the shape factor is close to 1.4, i.e. hardly changed compared to the ZPG case without VGs, but decreases to a minimum value below 1.3 around 1.5 m behind the array, where it starts to recover. A similar evolution of the shape factor was reported by Fransson *et al.* (2005) in a laminar boundary layer. Here, the interesting result is that in an averaged perspective the yaw does not affect the shape factor or the change of VG size (only moderately) as shown in figure 23.

When a VG pair is yawed the absolute angle of attack of one blade increases, while the angle of attack of the other blade decreases. Thus one of the vortices in the counter-rotating pair becomes stronger, and the other gets weaker. Due to the shear flow and possible blade separation it is not clear whether this is a linear process at both blades, and therefore it is difficult to predict the total circulation generated by the VG pair. This investigation shows that the total circulation, up to a yaw angle of 20°, is almost constant (see figure 24*a*). The circulation decay (seen vertically in the figure) also seems to be independent of yaw.

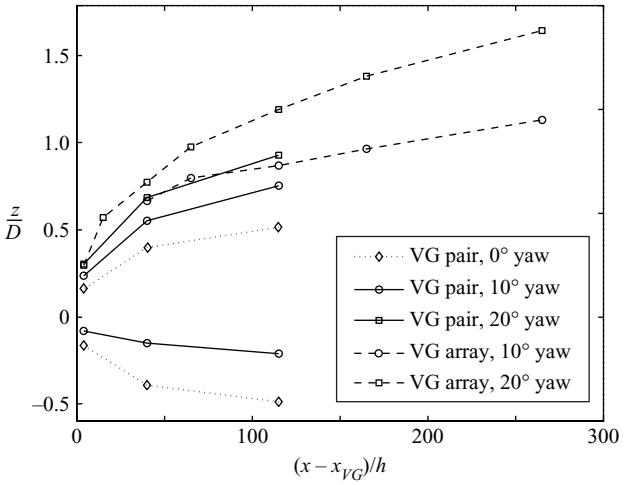

FIGURE 25. Vortex centre paths of VG_{10} pairs and arrays at 0°, 10° and 20° yaw.

In figure 24(*b*) the effect of yaw on the individual vortices in a VG pair is shown at $(x-x_{VG})/h=6$. At 0° the two vortices should be of equal strength. The difference in the figure is due to imperfect positioning and manufacturing of the VG and to some degree also due to measurement error. When the yaw angle increases the circulation of both vortices changes linearly, and according to the figure the blade that is parallel to the flow ($\beta=15°$) still produces a vortex. The reason for this behaviour could be that the strong vortex deflects the flow to reach the parallel blade at some angle or that this is caused by vorticity induced by the larger vortex. As shown by Wendt (2001) the circulation generated by a VG blade keeps increasing even after the blade stalls. This is probably what we observe here, since at 20° of yaw, i.e. an angle of attack of 35° of the strong vortex, the flow has most likely separated from the low-pressure side of the blade.

Furthermore, the vortex centre paths are changed at yaw, which could be observed already in figure 22. This is due to the asymmetry caused by the fact that the two vortices of a pair are of different strength. In the 0° yaw case there is no net side force, but as soon as there is a difference in circulation the mirror images will induce a velocity that modifies the vortex paths. The paths are deflected in the direction of the strong vortex, and in figure 25 the vortex centre paths for different yaw angles are shown. When one of the vortices from the VG pair disappears, there is no longer a pair or an array of counter-rotating vortices. In the case of a VG pair the result is a single longitudinal vortex. An array of VG pairs at yaw will produce a system of co-rotating vortices. Since the induced velocities of all the mirror images of the array work in the same direction the deflection angle is larger for an array compared to a pair at the same yaw angle. The vortex centre path of a VG pair at 20° yaw is approximately the same as that of a vortex generated in an array at 10° yaw. For the VG pair it was only possible to track the paths of the vortices up to $(x-x_{VG})/h=116$; beyond this position they were deflected out of the measurement plane due to the limited spanwise range of the traversing system. In case of the array it was possible to combine the vortex paths that were going out of the plane with the ones coming in from the other side.

5. A pseudo-viscous vortex model

In the course of this paper potential flow theory has been used to explain the streamwise evolution of longitudinal vortices. Jones (1957) calculated the paths of counter-rotating vortices from a system of VGs, using potential flow theory, and Pearcy (1961) proposed design criteria of VGs based on these calculations. Even though the assumption that the effect of viscosity can be neglected, implying that there is no wall-normal shear due to the slip condition at the wall and consequently that the vortices do not decay in strength as they move downstream, the agreement with experiments is remarkably good in the near region of the VG array. In this experiment measurements have been performed as far downstream as $450h$ of the VG array, and it is clear that the assumptions become questionable. However, here we have extended the analysis by Jones to also include vortex strength decay and a streamwise asymptotic z/D limit of the vortex centre based on experimental observations. This improved model seems to capture the effects of the flow physics in order to describe the vortex path also in the far region and, thus, gives a satisfactory agreement with the experimental results throughout the measurement region.

Jones (1957) showed that the projected vortex path in the plane normal to the stream is given by

$$\operatorname{cosech}^2\eta + \operatorname{cosec}^2\xi = C, \tag{5.1}$$

where $\xi = 2\pi z/D$, $\eta = 2\pi y/D$, and C is a constant determined from the coordinates of the VG pair tips ($\xi_1,\ \eta_1$). From simple geometry analysis of the present VGs these coordinates are $(\xi_1,\ \eta_1) = (\pi[d/D + l/D\ \tan\ \alpha],\ 2\pi h/D)$ giving $C = C_0 = 3.89$ (cf. table 2). Moreover, the slopes of the paths projected in the x–z and x–y planes were also deduced by Jones and are given by

$$\frac{\mathrm{d}\xi}{\mathrm{d}\theta} = \frac{k\ \tan^2\xi}{\sinh\ 2\eta\ (\tan^2\xi + \tanh^2\eta)} \tag{5.2}$$

and

$$\frac{\mathrm{d}\eta}{\mathrm{d}\theta} = \frac{k\ \tanh^2\eta}{\sin\ 2\xi\ (\tan^2\xi + \tanh^2\eta)}, \tag{5.3}$$

respectively, where $\theta = 2\pi x/D$ and $k = \{k_0 = \Gamma_0/(D \cdot U_h)\} = \text{constant}$ is the dimensionless vortex strength at the VG tips. These equations can be integrated stepwise after substituting for η or ξ from (5.1). For continuously increasing ξ and η, once one of the two integrals (from (5.2) or (5.3)) has been calculated, the path projected in the missing plane is known, indirectly, through (5.1). Worth mentioning here is since the applied VGs are 'self-similar' there is no difference between the array configurations, and thus their vortex centers follow the same paths.

Jones (1957) estimated the magnitude of k by a form of 'lifting-line-theory', and hence k becomes solely a function of the incidence angle and configuration of the VGs (i.e. chord length, tip locations ($\xi_1,\ \eta_1$) and the lift slope in two-dimensional flow). However, the experiments (figure 16) show that the vortex strength decays exponentially with x, i.e. $k = k(\theta)$, and is not a constant. Thus, in the extended model we let k vary as $\exp\{-\sigma \times 10^{-2}(x - x_{VG})/h\}$ with $\sigma = 3.24$, as shown in figure 26(a), where k_0 is estimated from the experimental data to be 0.19 in the limit when x goes to zero. Here, the exponent has been tuned to fit the data, and a comparison with the measured vortex strength decay (figure 16) reveals

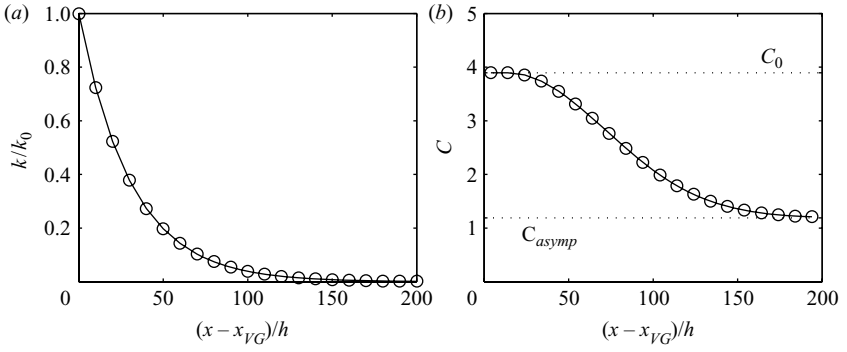

FIGURE 26. Model functions for (*a*) the vortex strength decay and (*b*) the variable C in (5.1).

that a stronger decay is needed for the model to work well in the far region. However, the choice of the exponential constant σ can be seen as a calibration parameter.

According to (5.1) the cross-flow vortex path is independent of k, and for increasing η the vortex core asymptotes to a constant ξ value, which is already set by the initial VG configuration since $C = C_0 =$ constant. However, the experimental data show that the position of vortex core levels off to a constant wall-normal distance at the same time as the cores from a VG pair (in the array) move towards each other. In order to capture this behaviour with the model one needs to allow C to vary with θ. Now, we can make use of the previously discussed asymptotic core limits (see § 3.3), namely $(\xi_{asymp}, \eta_{asymp}) = (1.57, 1.57)$, which gives $C_{asymp} = 1.19$, and assume C to vary as $\exp\{\varphi(\theta - \theta_s)^2\}$ between C_0 and C_{asymp} (see figure 26*b*). Here, θ_s and φ were set to 14 and 1.5×10^{-4}, respectively, and can be seen as another set of calibration parameters of the model.

Figure 27 compares Jones's (1957) original model and the pseudo-viscous model with experimental data for the three projected planes. In (*a*) the near region, up to $(x - x_{VG})/h = 45$, for the x–z plane is shown. The dashed lines correspond to the smoke visualization results, which rather represent the position of maximum positive mean velocity of the wall-normal component and then the location of the vortex cores. It is seen that the dashed lines diverge from the measured data points in the downstream direction, which is an artefact of the vortex growth. However, already at $(x - x_{VG})/h$ of about 30 the neighbouring vortices limit the growth in the spanwise direction. In figure 27(*a*) it is seen that both models work well in the near region of the VGs. However, since Jones's (1957) model does not allow for a variation in C the vortex path reaches its asymptotic spanwise equidistance around $(x - x_{VG})/h = 30$ and consequently fails to describe the core evolution beyond this location (see figure 27*c*). In figure 27(*d*) the x–y plane is shown. The dotted line corresponds to the slope $\mathrm{d}\eta/\mathrm{d}\theta$ (5.3) in the limit when η goes to infinity. It is seen that Jones's (1957) model is unable to predict the correct behaviour beyond $(x - x_{VG})/h$ around 25, suggesting that the vortices, in quite an unphysical way, take off from the wall with a constant slope. However, the pseudo-viscous model works fine due to the vortex strength decay implementation. Finally, the peculiar curving-back motion of the vortex cores in the cross-flow plane is captured by the pseudo-viscous model as can be seen in figure 27(*b*).

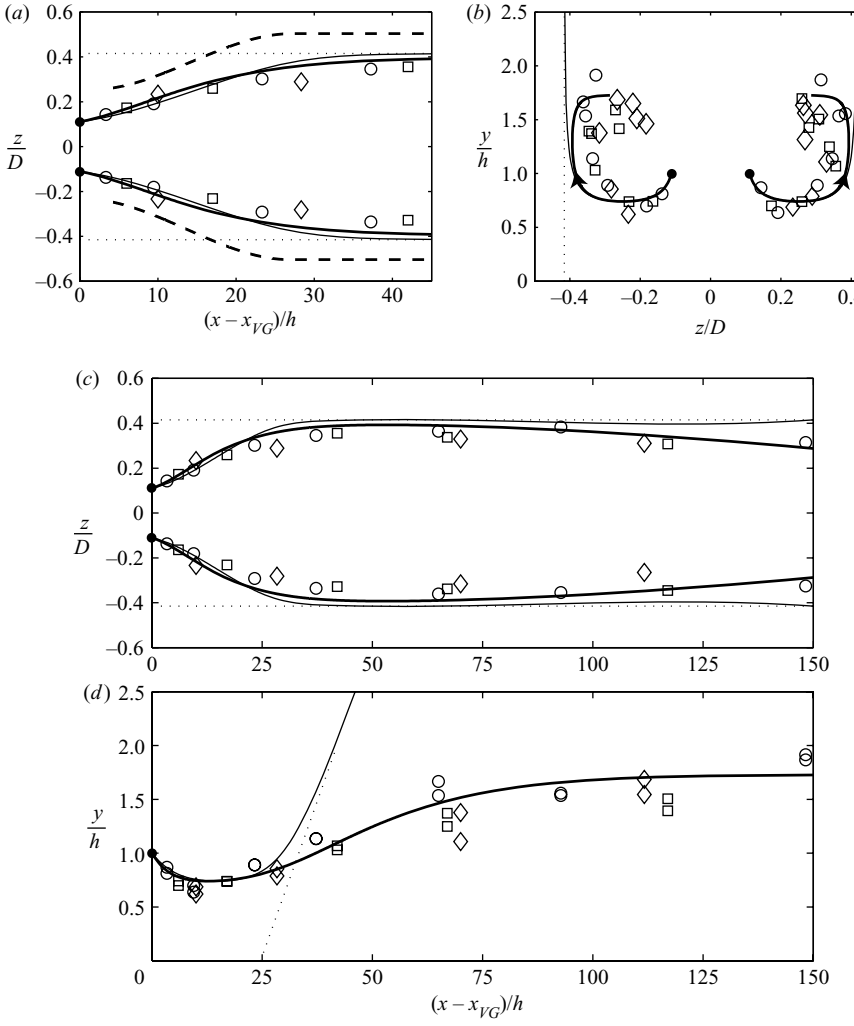

FIGURE 27. (*a–d*) The vortex paths in the three projected planes. Bullets correspond to the positions of the VG tips; dotted lines indicate asymptotic limits for Jones's (1957) original model; solid lines are theoretical curves, where the bold lines correspond to the pseudo-viscous model and the thin lines to Jones 's (1957) model. The bold dashed lines in (*a*) correspond to the flow visualization results. For the open symbols cf. table 2.

6. Conclusions

In this study, in which both smoke visualization and hot-wire anemometry have been used, several new results of the evolution of longitudinal vortices are reported. Both vortex pairs and vortex arrays in the natural setting as well as yawed have been studied. A comparison between the smoke visualization and hot-wire data affirm that, as intuitively expected, the trace of cumulative smoke particles in the laser sheet rather corresponds to the position of maximum positive vertical mean velocity than the location of the vortex core. Moreover, it is shown that for the present similarity parameter $D/h = 8.33$ there is no substantial difference between the pair and the array vortex core evolution up to $(x - x_{VG})/h$ of about 35.

The vortex core paths in plan view as well as in the plane parallel to the stream scale with the VG height in the downstream direction and with D and h in the spanwise and wall-normal directions, respectively. In the array case the vortex paths are locked in the spanwise direction due to the neighbouring vortex pair, and consequently the proposed scaling works better in the far region for this configuration compared to the VG pair case. In this paper an asymptotic limit hypothesis of the vortex array path is stated and is shown to hold reasonable well. The limiting values are $(y/h, z/D) = (2.08, \pm 0.25)$, which the experimental data seem to approach. This result is contradictory to the inviscid flow analysis put forward by Jones (1957). Furthermore a peculiar hooklike motion, not previously reported, of the vortex core in the cross-sectional plane has been found in the array case as well as in the VG pair case. This motion is explained by the vortex growth and the limiting space inside the boundary layer due to neighbouring vortices. It is here shown, in the VG pair case, that strong vortices are able to induce vorticity which is rolled up into a secondary vortex and hence affect the primary vortex path. These flanking secondary vortices, naturally present in the VG array configuration, are responsible for the hooklike motion in the VG pair case, which otherwise would be absent. Furthermore, it has been shown that in both the pair and the array configuration the circulation decays exponentially with about the same rate, and the circulation scales with the VG height and corresponding local velocity at the position of the VG tip.

A striking result regarding the turbulence quantities is how well they scale with the VG height in the streamwise direction (cf. § 3.5).

The results of the yawed configurations are that in an averaged perspective there is hardly any effect compared with the natural setting. We have shown that the spanwise-averaged shape factor is unaffected by yaw as well as the spanwise-averaged circulation. The stronger vortex in a yaw configuration compensates for the weaker contribution of the coupled vortex, thus rendering out the averaged effect. A notable difference between the natural setting and the yawed lies in the vortex core paths, which becomes important if a successive array or pair is thought of being implemented for a more persistent streamwise modulation of the base flow. It has been shown that the asymmetry affects the array configuration more than the pair case by comparing the 10° array yaw with the 20° single pair yaw, which show a similar streamwise evolution. Furthermore, as soon as the symmetry is broken due to yaw the asymptotic limit hypothesis ceases to be valid, since the paths are continuously deflected in the spanwise direction in favour for the stronger vortex. The weaker vortex with less circulation is not lifted up as strongly as its coupled vortex, and consequently the weaker vortex core stays closer to the wall compared to the stronger vortex.

In order to capture the evolution of vortex core paths in the far region behind an array of counter-rotating vortices it has been shown through a pseudo-viscous vortex model that circulation decay and streamwise asymptotic limits have to be taken into account. These two viscous effects seem to contain the necessary physics for a model to perform well also in the far field. Based on a rather simple inviscid analysis by Jones (1957) an extended version is here proposed in which the two viscous effects just mentioned have been incorporated. Comparing the pseudo-viscous vortex model with the experimental data gives a satisfactory agreement throughout the measured region down to $400h$. Involved in the model are three calibration/tuning parameters. One is the exponential constant σ giving the circulation decay, and the other two are connected to the model function $C(\theta)$ appearing as a constant in the inviscid analysis (cf. (5.1)). Experimental data analysis of VG arrays has shown that the vortex core evolution scales with the VG height (h) and the individual VG pair spacing (D) in

the streamwise and spanwise directions, respectively. Furthermore, the wall-normal position also scales with the VG height. Since the starting point for the pseudo-viscous vortex model is a purely inviscid model, i.e. boundary layer independent, the newly developed pseudo-viscous model also does not depend on the boundary layer parameters. In addition, since the analysis shows that the circulation of the VGs scale with the VG height and the corresponding velocity at that height, we believe that the initial vortex strength generated at the VG tip would scale equally good with the VG blade angle (α). The vortex path in both the x–z and x–y planes would in turn be well predicted by the pseudo-viscous vortex model due to the locking effect in the spanwise direction, which is created by the neighbouring VGs. No other parameter is likely to have any significant effect on the streamwise vortex core evolution, meaning that the model is robust to geometry changes.

Ola Lögdberg acknowledges Scania CV for the opportunity to carry out his doctoral work at KTH Mechanics within the Linné Flow Centre.

REFERENCES

Angele, K. P. & Muhammad-Klingmann, B. 2005 The effect of streamwise vortices on the turbulence structure of a separating boundary layer. *Eur. J. Mech.* B **24**, 539–554.

Blackwelder, R. F. & Eckelmann, H. 1979 Streamwise vortices associated with the bursting phenomenon. *J. Fluid Mech.* **94**, 577–594.

Cutler, A. D. & Bradshaw, P. 1991 A crossed hot-wire technique for complex turbulent flows. *Exp. Fluids* **12**, 17–22.

Fransson, J. H. M., Brandt, L., Talamelli, A. & Cossu, C. 2005 Experimental study of the stabilization of Tollmien–Schlichting waves by finite amplitude streaks. *Phys. Fluids* **17**, 054110.

Fransson, J. H. M., Talamelli, A., Brandt, L. & Cossu, C. 2006 Delaying transition to turbulence by a passive mechanism. *Phys. Rev. Lett.* **96**, 064501.

Godard, G. & Stanislas, M. 2006 Control of a decelerating boundary layer. Part 1: Optimization of passive vortex generators. *Aero. Sci. Technol.* **10**, 181–191.

Hunt, J. C. R., Wray, A. A. & Moin, P. 1988 Eddies, streams, and convergence zones in turbulent flows. In *Studying Turbulence using Numerical Simulation Databases-II* (eds Moin, P., Reynolds, W. C. & Kim, J.). Proc. 1988 Summer Program, *Center for Turbulence Research Report CTR-S88*, p. 193.

Jeong, J. & Hussain, F. 1995 On the identification of a vortex. *J. Fluid Mech.* **285**, 69–94.

Johansson, A. V. & Alfredsson, P. H. 1982 On the structure of turbulent channel flow. *J. Fluid Mech.* **122**, 295–314.

Jones, J. P. 1957 The calculation of the paths of vortices from a system of vortex generators, and a comparison with experiment. *Tech Rep.* C. P. No. 361. Aeronautical Research Council.

Lin, J. C. 2002 Review of research on low-profile vortex generators to control boundary-layer separation. *Prog. Aero. Sci.* **38**, 389–420.

Lindgren, B. & Johansson, A. V. 2002 Evaluation of the flow quality in the MTL wind-tunnel. *Tech Rep.* 2002:13. Department of Mechanics, KTH, Stockholm.

Lögdberg, O. 2006 Vortex generators and turbulent boundary layer separation control. Licentiate thesis, Department of Mechanics, KTH, Stockholm.

Mehta, R. D. & Bradshaw, P. 1988 Longitudinal vortices imbedded in turbulent boundary layers. Part 2. Vortex pair with 'common flow' upwards. *J. Fluid Mech.* **188**, 529–546.

Österlund, J. M. 1999 Experimental studies of a zero pressure-gradient turbulent boundary layer flow. PhD thesis, Department of Mechanics, KTH, Stockholm.

Österlund, J. M., Johansson, A. V., Nagib, H. M. & Hites, M. H. 2000 A note on the overlap region in turbulent boundary layers. *Phys. Fluids* **12**, 1–4.

Pauley, Wayne R. & Eaton, John K. 1988 Experimental study of the development of longitudinal vortex pairs embedded in a turbulent boundary layer. *AIAA J.* **26**, 816–823.

Pearcy, H. H. 1961 *Boundary Layer and Flow Control: Its Principle and Applications*, vol. 2. Pergamon.

Schubauer, G. B. & Spangenberg, W. G. 1960 Forced mixing in boundary layers. *J. Fluid Mech.* **8**, 10–32.

Shabaka, I. M. M. A., Mehta, R. D. & Bradshaw, P. 1985 Longitudinal vortices imbedded in turbulent boundary layers. Part 1. Single vortex. *J. Fluid Mech.* **155**, 37–57.

Swearingen, J. D. & Blackwelder, R. F. 1987 The growth and breakdown of streamwise vortices in the presence of a wall. *J. Fluid Mech.* **182**, 255–290.

Taylor, H. D. 1947 The elimination of diffuser separation by vortex generators. *Tech Rep.* R-4012-3. United Aircraft Corporation.

Tsuji, Y., Fransson, J. H. M., Alfredsson, P. H. & Johansson, A. V. 2007 Pressure statistics and their scaling in high-Reynolds-number turbulent boundary layers. *J. Fluid Mech.* **585**, 1–40.

Watmuff, J. H., Witt, H. T. & Joubert, P. N. 1985 Developing turbulent boundary layers with system rotation. *J. Fluid Mech.* **157**, 405–448.

Wendt, Bruce J. 2001 Initial circulation and peak vorticity behavior of vortices shed from airfoil vortex generators. *Tech Rep.* NASA/CR 2001-211144. NASA.

Wendt, B. J., Reichert, B. A. & Jeffry, D. F. 1995 The decay of longitudinal vortices shed from airfoil vortex generators. *Tech Rep.* 198356 AIAA-95-1797. NASA.

Westphal, R. V., Eaton, J. K. & Pauley, W. R. 1987 Interaction between a vortex and a turbulent boundary layer in a streamwise pressure gradient. In *Turbulent Shear Flows* **5** (ed. F. Durst, B. E. Launder, J. L. Lumley, F. W. Schmidt & J. M. Whitelaw), pp. 266–277. Springer.

Westphal, R. V. & Mehta, R. D. 1989 Interaction of an oscillating vortex with a turbulent boundary layer. *Exp. Fluids* **7**, 405–411.

Westphal, R. V., Pauley, W. R. & Eaton, J. K. 1987 Interaction between a vortex and a turbulent boundary layer. Part 1: Mean flow evolution and turbulence properties. *Tech Rep.* TM 88361. NASA.

Yao, C.-S, Lin, J. C. & Allan, B. G. 2002 Flow-field measurement of device-induced embedded streamwise vortex on a flat plate, *AIAA Paper* 2002-3162.